The Magnetotelluric Phase Tensor: A Critical Review

John R. Booker

Abstract   The magnetotelluric (MT) phase tensor is a property of the MT impedance that is resistant to a common form of distortion due to unresolvable local structure. Review of the theory leads to a new geometrical description that cleanly separates information about directionality and dimensionality of regional conductivity structure. This information is widely used to justify two-dimensional (2D) interpretation, but the case is seldom made convincingly. In particular, errors are largely ignored and it is not understood that full data covariance is essential for accurate error bars. It is also common to use 2D impedance tensor decompositions when the phase tensor shows this model to be inconsistent with the data. A phase tensor-consistent impedance tensor decomposition is introduced. Because the phase tensor is a distortion-free 3D response, it should be used as data for 3D inversions. Until codes for this become more developed, comparison of predicted and observed phase tensors can ascertain whether 3D aspects of the data have been adequately fit by other inversions or modeling.

Keywords   Magnetotelluric phase tensor · Dimensionality · Distortion · Impedance decomposition · Impedance covariance

1 Introduction

Magnetotelluric (MT) data sense electrical conductivity of Earth's interior and find application in a variety of contexts. These include exploration for economic resources when the conductivity of the target differs from its host and tectonic processes both active and ancient. MT is particularly useful when the target scale is large or deep because it uses natural time-varying electric and magnetic fields which are difficult to generate artificially over large areas and at long period. It is complementary to other geophysical techniques because conductivity depends strongly on interconnection of spatial transport properties.

J. R. Booker (✉)
Department of Earth and Space Sciences, University of Washington, Seattle, WA 98195, USA
e-mail: JohnRBooker@yahoo.com

MT is inherently more difficult than many remote sensing techniques because little can be learned about Earth's interior by looking at the raw time series which are dominated by processes in Earth's atmosphere and space environment. Additionally, Earth structure is commonly multi-dimensional and may be anisotropic.

A major step forward in the MT method was recognition that data were often distorted by unresolvable small-scale structure. This led to techniques to extract undistorted data. The most widely used assumes that large-scale structure is two-dimensional (2D). Caldwell et al. (2004) took a different approach and introduced the MT phase tensor which is unaffected by a common form of distortion and makes no assumptions about regional structure. Since then, Caldwell et al. have been cited by more than 80 papers.[1] The majority of applications involve justifying 2D interpretation. Few papers have taken further advantage of the information in the phase tensor and many papers simultaneously use techniques that violate constraints implied by the phase tensor.

This paper begins with a review of the theory that differs somewhat from Caldwell et al. It presents an alternate parameterization of the phase tensor that I find more intuitive than the original and more clearly separates directionality and dimensionality information. Because error estimation is critical to most applications and is widely ignored, I discuss it in some detail. I also describe how the phase tensor has been used (and abused) and discuss a way to generalize the 2D impedance tensor decompositions (Bahr 1988; Groom and Bailey 1989) that have dominated MT interpretation for the last two decades so they become compatible with the phase tensor. Finally, I review ways the phase tensor can contribute more widely to MT interpretation.

2 Geometry of the MT Phase Tensor

The relationship between the horizontal magnetic (**H**) and electric (**E**) field vectors at an MT site is normally represented in the frequency domain by

$$\mathbf{E} = \mathbf{Z}\mathbf{H} \tag{1}$$

The MT impedance tensor **Z** is a complex transfer function. In Cartesian coordinates (x, y, z), this can be written out

$$\begin{bmatrix} E_x \\ E_y \end{bmatrix} = \begin{bmatrix} Z_{xx} & Z_{xy} \\ Z_{yx} & Z_{yy} \end{bmatrix} \begin{bmatrix} H_x \\ H_y \end{bmatrix} \tag{2}$$

E and **H** are driven by quasi-stationary physical phenomena outside Earth, while **Z** is assumed to be a stable property of the subsurface electrical conductivity structure. Thus, (1) is a statistical model in which fluctuations of observed **Z** for different time windows of **E** and **H** are considered to be due to random fluctuations in the input fields. The details of how best to estimate **Z** and its uncertainties depend on whether the average external field can be represented as a plane wave, whether noise is in **E** or **H** or both and how non-Gaussian residuals are dealt with (Gamble et al. 1979; Egbert and Booker 1986, Chave et al. 1987; Chave and Thomson 1989; Jones et al. 1989; Egbert 1997; Chave 2012a). With one exception, this paper assumes that these issues have already been adequately addressed. The exception is that it will be shown that the full covariance matrix of **Z** is more important than generally appreciated and can be critical in phase tensor applications.

---

[1] A file of References can be obtained from a link at http://earthweb.ess.washington.edu/booker. A more up-to-date list can be generated using the Science Citation Index or GeoRef.

It is therefore essential that the time series processing code reports this important information, not just the standard errors.

Major issues in inverting estimates of $\mathbf{Z}$ for Earth structure are distortion of $\mathbf{Z}$ by unresolvable small-scale structure and the dimensionality and directionality of the underlying regional structure. The MT phase tensor is defined by

$$\boldsymbol{\Phi} = \mathbf{X}^{-1}\mathbf{Y} = \begin{bmatrix} \Phi_{xx} & \Phi_{xy} \\ \Phi_{yx} & \Phi_{yy} \end{bmatrix} \tag{3}$$

where $\mathbf{X}$ and $\mathbf{Y}$ are the real and imaginary parts of $\mathbf{Z}$ (Caldwell et al. 2004). The phase tensor has become an important tool because of three properties: First, $\boldsymbol{\Phi}$ does not change if $\mathbf{Z}$ is multiplied by any real two-by-two matrix (as when regional-scale impedance is distorted by local structure); second, its matrix skew is zero when the regional structure is 2D; and third, information about preferred orientation of regional structure is easily extracted.

It is worth emphasizing that $\boldsymbol{\Phi}$ is a property of $\mathbf{Z}$ that makes no assumptions about how the electric and magnetic fields interact with the structure. Existing applications assume that local structure does not significantly distort the horizontal magnetic field $\mathbf{H}$. An undistorted horizontal magnetic field is not always the case. Groom and Bailey (1991) show an example where this assumption fails and Chave and Smith (1994) extend 2D impedance tensor decomposition to include magnetic distortion. However, the geometry of $\boldsymbol{\Phi}$ exists independent of the assumption of undistorted $\mathbf{H}$ and has meaning when the magnetic field is distorted. Useful behavior of the phase tensor in the presence of magnetic distortion needs investigation.

This section reformulates the presentations of Caldwell et al. (2004) and Bibby et al. (2005). Bibby et al. add insights into Caldwell et al., but cover essentially the same material and involve the same authors. In most cases, I refer to these formative papers simply as Caldwell et al.

Consider a distorted horizontal electric field $\mathbf{E}_D$ that is related to an undistorted horizontal electric field $\mathbf{E}$ by

$$\mathbf{E}_D = \mathbf{D}\mathbf{E} \tag{4}$$

where the two-by-two "Distortion Matrix" $\mathbf{D}$ is real. $\mathbf{D}$ can always be interpreted as a rotation and a change of magnitude of the undistorted field. When $\mathbf{D}$ is due to deflection of "regional" electric current by small-scale electric charges in phase with the regional $\mathbf{E}$ field, $\mathbf{D}$ is period-independent and the distortion is termed "Galvanic" or "static" (Bahr 1988; Jiracek 1990). I will use the term "static."

To make further progress, it is necessary to assume that $\mathbf{D}$ is not singular. When $\mathbf{D}$ is singular, the direction of $\mathbf{E}_D$ becomes independent of the direction of $\mathbf{E}$ and one has no hope of extracting the undistorted field from distorted measurements. MT sites with singular $\mathbf{D}$ can be identified by electric signals on non-colinear dipoles that are 100 % correlated or finding a coordinate system in which one of the measured electric field components is zero.

Multiplying (1) by $\mathbf{D}$ and assuming that the horizontal magnetic field is not distorted gives

$$\mathbf{D}\mathbf{E} = \mathbf{D}\mathbf{Z}\mathbf{H} \equiv \mathbf{Z}_D\mathbf{H} \tag{5}$$

The distorted impedance in the same coordinate system as $\mathbf{Z}$ is seen to be

$$\mathbf{Z}_D = \mathbf{D}\mathbf{Z} = \mathbf{X}_D + i\mathbf{Y}_D = \mathbf{D}\mathbf{X} + \mathbf{D}\,(i\mathbf{Y}) \tag{6}$$

Relationship (6) is not immediately useful because there are 12 unknowns—4 elements of **D** and the real and imaginary parts of the 4 complex elements of **Z**, while there are only 8 measured data (the real and imaginary parts or the magnitudes and phases of the four complex distorted impedance elements). On the other hand, the phase tensor of the distorted impedance is easily seen to be independent of **D**:

$$\boldsymbol{\Phi}_D = \mathbf{X}_D^{-1}\mathbf{Y}_D = (\mathbf{DX})^{-1}\mathbf{DY} = \mathbf{X}^{-1}\mathbf{D}^{-1}\mathbf{DY} = \mathbf{X}^{-1}\mathbf{Y} = \boldsymbol{\Phi} \tag{7}$$

Its real elements constitute 4 undistorted data that are completely determined by the measured data.

Impedance can be transformed to a rotated coordinate system using

$$\mathbf{Z}_{\text{rot}} = \mathbf{RZR}^{-1} \tag{8}$$

where the unitary coordinate rotation operator for vectors is

$$\mathbf{R}(\theta) = \begin{bmatrix} \cos(\theta) & \sin(\theta) \\ -\sin(\theta) & \cos(\theta) \end{bmatrix} \tag{9}$$

Note that **R** rotates (in the right-hand sense) the *coordinate system* in which a vector is expressed, while $\mathbf{R}^{-1}$ rotates the vector itself in a *fixed coordinate system*. Note also that $\mathbf{R}^{-1}(\theta) = \mathbf{R}^{\text{T}}(\theta) = \mathbf{R}(-\theta)$ where the superscript T means transpose and that $\mathbf{R}(\theta_1)\mathbf{R}(\theta_2) = \mathbf{R}(\theta_2)\mathbf{R}(\theta_1)$, that is, multiple rotations can be performed in any order. I sometimes use the notation $\mathbf{R}_\theta = \mathbf{R}(\theta)$ when the rotation angle is not obvious from context. It is easy to show that $\boldsymbol{\Phi}_{\text{rot}}$ (the phase tensor in the rotated system) can be computed either from $\mathbf{Z}_{\text{rot}}$ or by rotating the coordinates of $\boldsymbol{\Phi}$.

2.1 Two-Dimensional Structure

As already noted, the action of any two-by-two real matrix such as $\boldsymbol{\Phi}$ on a vector is to rotate it and change its length. Applying the phase tensor (3) to a family of radial vectors $\mathbf{c}(\omega)$ whose tip circulates around a unit radius circle as the polar angle ω increases from 0 to 360° (see Fig. 1a) produces another family of radial vectors

$$\mathbf{p}(\omega) = \boldsymbol{\Phi}\,\mathbf{c}(\omega) = \begin{bmatrix} \Phi_{xx} & \Phi_{xy} \\ \Phi_{yx} & \Phi_{yy} \end{bmatrix} \begin{bmatrix} \cos(\omega) \\ \sin(\omega) \end{bmatrix} = \begin{bmatrix} \Phi_{xx}\cos(\omega) + \Phi_{xy}\sin(\omega) \\ \Phi_{yx}\cos(\omega) + \Phi_{yy}\sin(\omega) \end{bmatrix} = \begin{bmatrix} p_x(\omega) \\ p_y(\omega) \end{bmatrix} \tag{10}$$

Consider the anti-diagonal 2D impedance when the measurement axes x and y are aligned parallel and perpendicular to strike:

$$\mathbf{Z}^{2D} = \begin{bmatrix} 0 & Z_{xy} \\ Z_{yx} & 0 \end{bmatrix} \tag{11}$$

Its phase tensor is

$$\boldsymbol{\Phi}^{2D} = \begin{bmatrix} \tan(\phi_{yx}) & 0 \\ 0 & \tan(\phi_{xy}) \end{bmatrix} \tag{12}$$

where ϕ_{xy} and ϕ_{yx} are the phase angles of the complex impedance elements Z_{xy} and Z_{yx}. When the time dependence of the electromagnetic fields is $e^{+i\eta t}$ (where η is radian frequency and t is time), the phase of Z_{yx} is in the third quadrant between −180° and −90° while the phase of Z_{xy} is between 0 and 90°. Because $\tan(\phi_{yx} + 180°) = \tan(\phi_{yx})$, the
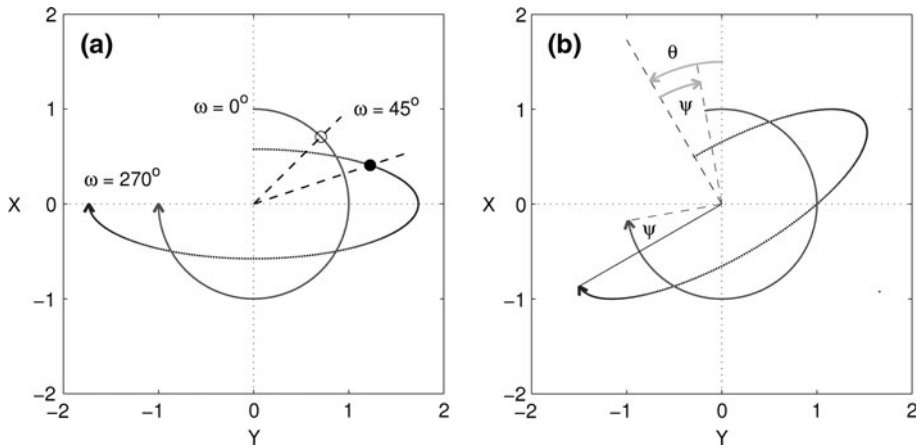
Fig. 1 Ellipses generated by applying a phase tensor to circulation around a unit circle. Only 270° of the circulation is shown and *arrow heads* show the sense of circulation. The *start* and end points for each *ellipse* correspond to the start and end points for each *circle*. **a** 2D impedance in a coordinate system aligned with the *x*- and *y*-axes. The minor axis corresponds to the phase of Z_{yx} and has length tan (30°). The major axis corresponds to the phase of Z_{xy} and has length tan (60°). The *open point* at 45° on the unit *circle* corresponds to the filled point on the *ellipse*. The *radial dashed lines* through the two points are not colinear at this ω, but would be at the ellipse axes. **b** 3D impedance with the same size phase tensor ellipse. The normalized skew angle $\psi = 20°$ and impedance *x*-axis are rotated $-30°$ from the *x*-axis

upper left element of $\mathbf{\Phi}^{2D}$ cannot distinguish whether ϕ_{yx} is in the third or first quadrant. Thus, the elements of the phase tensor are equal to each other when the structure is 1D.

Substituting (12) in (10) gives

$$\mathbf{p}^{2D}(\omega) = \mathbf{\Phi}^{2D}\mathbf{c}(\omega) = \begin{bmatrix} \tan(\phi_{yx}) & 0 \\ 0 & \tan(\phi_{xy}) \end{bmatrix} \begin{bmatrix} \cos(\omega) \\ \sin(\omega) \end{bmatrix} = \begin{bmatrix} \tan(\phi_{yx})\cos(\omega) \\ \tan(\phi_{xy})\sin(\omega) \end{bmatrix} \quad (13)$$

This is a parametric equation of an ellipse whose axes are along the *x* and *y* coordinate axes. The ellipse can be visualized by plotting the points ($|\mathbf{p}(\omega_i)|$, ω_i) in polar coordinates for ω_i distributed between 0 and 360° (see Fig. 1a). Note the right-handed coordinate system common in geomagnetism with *x* north, *y* east, *z* down, and positive rotation clockwise (i.e., east of north). A semi-axis extends outside the unit circle when the phase it represents has a tangent greater than unity, but remains inside the unit circle when the phase it represents has a tangent less than unity. The ellipse semi-axis in the *x* direction has length $\tan(\phi_{yx})$ and is consequently associated with the electric field in the *y* direction. The semi-axis in the *y* direction has length $\tan(\phi_{xy})$ and is associated with the electric field in the *x* direction. Thus, each ellipse axis is *perpendicular* to the polarization of its associated electric field.

2.2 Three-Dimensional Structure

2.2.1 The General Case

Any two-by-two matrix with real elements produces an ellipse when applied to the unit circle. If the matrix is singular, the ellipse degenerates to a line segment. Singular $\mathbf{\Phi}$ occurs when $\mathbf{Z}$ causes the electric field $\mathbf{E}$ to point in one direction regardless of the polarization of

H and, as in the case of singular **D**, one cannot extract useful structural information. In the 2D case just described, the vectors $\mathbf{p}^{2D}$ and **c** point in the same direction only when $\mathbf{p}^{2D}$ is an axis of the ellipse (see Fig. 1a). Thus, a point circulating around the unit circle crosses each axis of the ellipse exactly when the point circulating around the ellipse crosses the same axis. When **Φ** is not symmetric, however, the ω at which the point circulating around the unit circle crosses each ellipse axis is not the same as the ω at which the point circulating around the ellipse touches the ends of the semi-axes. Asymmetric phase tensor matrices are characteristic of impedances generated by 3D structure. A 3D phase tensor ellipse with the same size ellipse as Fig. 1a is shown in Fig. 1b.

It should be clear from Fig. 1b that the family of vectors **c** has been rotated through an angle ψ relative to the axes of the ellipse. When ψ is positive, the point circulating clockwise around the ellipse is observed to *lag behind* the point circulating clockwise around the unit circle. Remembering that $\mathbf{R}(\psi)$ defined by (9) rotates a vector in the counterclockwise direction when ψ is positive, this circulation lag can be expressed by

$$\mathbf{p}(\omega) = \mathbf{\Phi}_{\text{ellipse}}\,\mathbf{c}(\omega) = \begin{bmatrix} \Phi_a & 0 \\ 0 & \Phi_b \end{bmatrix} \mathbf{R}(\psi)\mathbf{c}(\omega) \tag{14}$$

where $\mathbf{\Phi}_{\text{ellipse}}$ is the phase tensor in the coordinate system aligned with the ellipse axes ("ellipse coordinates") and $|\Phi_a|$ and $|\Phi_b|$ are the lengths of the two ellipse semi-axes. It is then obvious from (14) that a completely general parameterization of a phase tensor in ellipse coordinates is

$$\mathbf{\Phi}_{\text{ellipse}} = \begin{bmatrix} \Phi_a & 0 \\ 0 & \Phi_b \end{bmatrix} \mathbf{R}(\psi) \tag{15}$$

If θ_{ellipse} is the angle between one of the measurement system axes and one of the phase tensor ellipse axes, the phase tensor in measurement coordinates can finally be parameterized by

$$\mathbf{\Phi} = \mathbf{R}^{-1}(\theta_{\text{ellipse}}) \begin{bmatrix} \Phi_a & 0 \\ 0 & \Phi_b \end{bmatrix} \mathbf{R}(\psi)\,\mathbf{R}(\theta_{\text{ellipse}}) \tag{16}$$

2.2.2 Normalized skew

The angle ψ is easily determined. Using (9), (15) can be rewritten

$$\mathbf{\Phi}_{\text{ellipse}} = \begin{bmatrix} \Phi_a & 0 \\ 0 & \Phi_b \end{bmatrix} \begin{bmatrix} \cos(\psi) & \sin(\psi) \\ -\sin(\psi) & \cos(\psi) \end{bmatrix} = \begin{bmatrix} \Phi_a\cos(\psi) & \Phi_a\sin(\psi) \\ -\Phi_b\sin(\psi) & \Phi_b\cos(\psi) \end{bmatrix} \tag{17}$$

The ratio of the matrix skew (difference of the off-diagonal elements) of $\mathbf{\Phi}_{\text{ellipse}}$ to its trace (sum of the diagonal elements) is

$$\frac{\Phi_a\sin(\psi) + \Phi_b\sin(\psi)}{\Phi_a\cos(\psi) + \Phi_b\cos(\psi)} = \left(\frac{\Phi_a + \Phi_b}{\Phi_a + \Phi_b}\right)\frac{\sin(\psi)}{\cos(\psi)} = \tan(\psi) \tag{18}$$

The skew and trace of a matrix are rotational invariants. So their ratio is also a rotational invariant and ψ can be computed from the phase tensor elements in *any coordinate system*. In particular, it can be computed in measurement coordinates. Thus, if (x, y) are identified as the measurement coordinate axes,

$$\psi = \tan^{-1}\left(\frac{\Phi_{xy} - \Phi_{yx}}{\Phi_{xx} + \Phi_{yy}}\right) \tag{19}$$

Since $\tan(\psi)$ is the matrix skew "normalized" by its trace, a natural name for ψ is the "normalized skew angle." It is twice the skew angle "β" introduced by Caldwell et al. and I use a different name and symbol to avoid confusion. It is obvious from (12) and (15) that ψ is zero when the structure is 2D and that $\theta_{ellipse}$ is the strike (or its perpendicular). However, $\psi = 0$ is not a sufficient condition for the structure to be 2D. On the other hand, $\psi \neq 0$ is a sufficient condition for the structure to be either 3D or, as we shall see shortly, have azimuthal anisotropy that varies with position.

2.2.3 Quasi-2D

2D structure requires zero ψ within its uncertainties. Accurate estimation of uncertainty is therefore critical if ψ is to be used to justify a 2D interpretation. Error estimation is discussed in Appendix 1. In summary, the so-called delta method for computing uncertainties of nonlinear functions of random variables is adequate for impedances whose errors are usefully small, while so-called Monte Carlo methods can fail unless great care is taken. Neglect of impedance element covariance can lead to error estimates that are much too large. Furthermore, strong static distortion leads to large impedance element covariance. It is consequently important to use codes for estimating $\mathbf{Z}$ that provide the full covariance matrix (for example, Egbert 1997).

A less stringent way to justify 2D interpretation is to examine the size of the 3D part of the phase tensor. When ψ (expressed in radians) is small, $\cos(\psi) \approx 1$ and $\sin(\psi) \approx \psi$. Then,

$$\mathbf{R}(\psi) \approx \begin{bmatrix} 1 & \psi \\ -\psi & 1 \end{bmatrix} \tag{20}$$

$$\mathbf{\Phi}_{ellipse} \approx \begin{bmatrix} \Phi_a & 0 \\ 0 & \Phi_b \end{bmatrix} \begin{bmatrix} 1 & \psi \\ -\psi & 1 \end{bmatrix} = \begin{bmatrix} \Phi_a & \psi\Phi_a \\ -\psi\Phi_b & \Phi_b \end{bmatrix} \tag{21}$$

The regional impedance that generated $\mathbf{\Phi}_{ellipse}$ is defined as "quasi-2D" if $|\psi|$ is small enough that the off-diagonals on the right side of (21) can be ignored. Note that $\sin(180° - |\psi|) = -\sin(|\psi|)$. Thus, skew angles near $\pm180°$ result in off-diagonal elements of similar small magnitude as angles near 0°. There is probably no rigorous bound for how far $|\psi|$ can be from 0° before 2D interpretation of quasi-2D impedance becomes invalid, but a useful criterion is that the phase tensor off-diagonals be an order of magnitude smaller than the diagonals. This implies $|\psi| \leq 0.1$ radians or less than 6°. This is in agreement with the recommendation of Caldwell et al. that their $|\beta|$ be less than 3°. Unfortunately, maximum permissible skew angle "inflation" has occurred in publications and few papers are as conservative as Caldwell et al. There are even authors who use $\beta = 10°$ ($\psi = 20°$) as an acceptable upper limit. A normalized skew this large implies off-diagonals of $\mathbf{\Phi}_{ellipse}$ one-third as big as its diagonals. Ignoring diagonals this large may have serious consequences.

Large skew angle is a robust test for 3D regional structure, but small skew angle is only a necessary but not sufficient test for quasi-2D, because 3D symmetry can locally make ψ small. It should also be emphasized that ψ can be in any quadrant. Appendix 1 includes an example with $\psi > 90°$ that has the additional complication of ellipse circulation in the direction opposite to the circulation about the unit circle. It is therefore important to use an

inverse tangent function that preserves the quadrant when computing ψ (atan2 in most programming languages).

2.2.4 Invariants of the Phase Tensor and Generalized Strike

Expressed in the form (16), the phase tensor consists of three parameters ψ and the lengths of the ellipse axes $|\Phi_a|$ and $|\Phi_b|$ that do not depend on the coordinate system in which they are evaluated. The ellipse axis direction θ_{ellipse} (or its perpendicular) is the electrical strike in 2D. Bibby et al. (2005) state that the ellipse axes should be parallel to the directions of greatest and least inductive response in 3D. They do not explain why or whether they think this is true for strongly 3D structure, but it is verified using numerical modeling by Caldwell et al. (2004) for skew angles small enough to be quasi-2D and definitely holds as long as the induction vectors are parallel to ellipse axes (within their uncertainties). For strong three dimensionality, the ellipse axes are vectors whose directions relative to the structure are fixed, although θ_{ellipse} depends on the reference coordinate system in which the conductivity structure is described. The ellipse axes are the only directional property of $\mathbf{Z}$ that is free of static distortion and thus one of them can be defined as the generalized strike. Because the phases corresponding to the ellipse axes approach the TE and TM mode phases as ψ approaches zero, it is reasonable to think of the electric current flow in the direction of the ellipse axes as being TE-like and TM-like. The TE analogy must break down before the TM one because current flow along a conductivity gradient always generates noninductive (i.e., Galvanic) electric fields which are not present in the TE mode.

2.2.5 Singular-Value Decomposition

Parameterization (16) is a singular-value decomposition (SVD) of particularly simple form. The singular values Φ_a and Φ_b are the tangents of the "principal phase angles" ϕ_a and ϕ_b. The magnitudes of Φ_a and Φ_b are the lengths of the ellipse semi-axes. A complication is that unlike singular values computed with standard SVD algorithms, Φ_a and Φ_b need not be positive. Weidelt and Kaikkonen (1994) showed that TM phase responses of 2D models lie in the range 0–90° permitted by 1D models. Since 2D phase tensors have $\psi = 0$, the singular value corresponding to TM must be positive. Parker (2010), however, proves that 2D models exist whose TE mode phase responses are outside 0–90°. Key and Constable (2011) on the seafloor near a coast and Selway et al. (2012) near the edge of a sedimentary basin provide practical examples of this behavior. Both can be explained by the arrival of energy from below as well as above. Thus, in a strictly 2D situation, one of the singular values can be negative and its principal phase can be out of quadrant. It is not yet known whether 3D models exist in which both singular values are negative.

Simple algorithms for computing the parameters in (16) and their uncertainties that do not have the ambiguities of Caldwell et al. (2004) discussed by Moorkamp (2007) and Caldwell et al. (2007) are presented in Appendix 1. A full discussion of using the phase tensor geometry to determine the quadrants of the principal phases is also presented in Appendix 1.

2.2.6 Other Parameterizations

Equation (16) is equivalent to Eq. (20) of Caldwell et al. (2004) and Eq. (16) of Bibby et al. (2005):

$$\boldsymbol{\Phi} = \mathbf{R}^{-1}(\alpha - \beta) \begin{bmatrix} \Phi_{\max} & 0 \\ 0 & \Phi_{\min} \end{bmatrix} \mathbf{R}(\alpha + \beta) \qquad (22)$$

with $\beta = \psi/2$ and $\alpha = \theta_{\text{ellipse}} + \psi/2$. However, unlike (16), the parameters in (22) do not all have an immediate intuitive interpretation. Specifically, angle α mixes the ellipse orientation (the generalized regional strike) with the measure of three dimensionality and has been wrongly identified as the regional strike in a significant number of papers. Fortunately, the error in using α instead of $\alpha - \beta$ as the strike is typically small enough that the conclusions of the offending papers are probably not seriously compromised.

Another disadvantage of (22) is ordering the size of the principal values and by implication assuming that they are positive (an automatic result of standard SVD algorithms). Sorting out the quadrants of the angles from such an SVD can be confusing especially since SVDs are not unique. The techniques of Appendix 1 make identifying the correct quadrants easy. First, find θ_{ellipse} closest to true North at one period and then require it to vary continuously with period. It is then easy to follow principal phase curves when they cross and distinguish crossing from the case where the phase curves only touch. Similarly, it is easier to judge whether 90° ellipse rotations at the same period between two sites are the consequence of a 90° rotation of strike (a serious 3D effect) or simply the crossing of principal phase curves at different periods with no change in strike (which can happen in a completely 2D situation).

Bibby et al. (2005) additionally define the phase tensor ellipticity

$$\lambda = \frac{|\Phi_a - \Phi_b|}{\Phi_a + \Phi_b}$$

This is the ellipticity of the phase tensor ellipse. In my opinion, the "principal phase split" angle $\Phi_a - \Phi_b$ is simpler and equally informative.

Weaver et al. (2004, 2006) present another interesting parameterization:

$$\boldsymbol{\Phi} = \begin{bmatrix} J_1 & 0 \\ 0 & J_1 \end{bmatrix} + J_2 \begin{bmatrix} \cos 2\alpha & \sin 2\alpha \\ \sin 2\alpha & -\cos 2\alpha \end{bmatrix} + \begin{bmatrix} 0 & J_3 \\ -J_3 & 0 \end{bmatrix} \qquad (23)$$

where α is the same as in (22), J_1 is the trace of $\boldsymbol{\Phi}/2$, J_3 is the matrix skew of $\boldsymbol{\Phi}/2$, and

$$J_2^2 = J_1^2 + J_3^2 - \det \boldsymbol{\Phi}$$

I have used the notation of Weidelt and Chave (2012) instead of the original which seems unnecessarily complicated. J_1, J_2, J_3, and the determinant of $\boldsymbol{\Phi}$ are rotational invariants and can be computed in any coordinate system. The utility in writing $\boldsymbol{\Phi}$ in this form is that only the first term is present for 1D structure, only the first and second terms are present for 2D structure and the third term is present only when the structure is 3D. The absence of the third term is completely equivalent to $\psi = 0$. Note that even though the matrix skew of the second term is always zero, it depends on the skew of $\boldsymbol{\Phi}$ because J_2 depends on J_3 and α depends on ψ. Thus, if we drop the third term when it is not zero, we are left with a 2D phase tensor that includes a correction for nonzero ψ. It would be definitely worthwhile doing 2D inversions of data generated by 3D structure to find out under what circumstances the principal phases of this 2D approximation are more useful estimates of TE and TM impedance phases than the principal phases of the original 3D phase tensor.

2.3 Anisotropic Conductivity

There is now a large body of the literature documenting tectonically caused seismic anisotropy and a growing literature interpreting MT phase splits ($\phi_{xy} - \phi_{yx}$) as evidence for electrical anisotropy in the same contexts (see Roux et al. 2011 for an example). Because static distortion mixes the phases of the perpendicular polarizations, it can easily generate impedance phase differences. It is therefore essential that an undistorted response such as the phase tensor be used to estimate the phase split. See Häuserer and Junge (2011) for an example.

Using the code of Pek and Santos (2002), Heise et al. (2006) demonstrate that phase tensor principal phase splits for 1D structure are generated by vertical gradients of anisotropy not by the anisotropy itself. Thus, circular phase tensor ellipses with no phase split are not a sufficient argument against 1D anisotropy.

Impedance of a 1D anisotropic Earth always takes the form

$$\mathbf{Z}^{1Da} = \begin{bmatrix} Z_d & Z_{xy} \\ Z_{yx} & -Z_d \end{bmatrix} \tag{24}$$

(see Jones 2012a). Because its trace is zero, the diagonal elements have equal magnitudes but opposite signs in any coordinate system. This is also true for a rotated isotropic 2D impedance. However, the phase tensor skew angle is also zero for 2D. So to eliminate isotropic 2D impedance as an alternative, one can simply show that ψ is not zero (within its uncertainty). This is better than the test suggested by Jones to show that the diagonal element Z_d is nonzero in all rotations because his test can break down completely if (24) is statically distorted.

The code of Pek and Santos can also be used to show that ψ is zero for $\mathbf{Z}^{1Da}$ if the *anisotropy strike* is constant with depth. Thus, nonzero phase tensor skew is a definitive indicator for depth variation of anisotropy direction if the alternative of isotropic 3D structure can be eliminated *in some other way*.

2.4 Displaying Phase Tensor Geometry

The goal of visualizing all the information in the phase tensor in a form compact enough to plot on pseudosections or maps remains unachieved. There are still no published examples that include the parameter errors except in single site plots of the parameters versus period. Clever ideas are clearly needed.

Figure 2 shows three ways of plotting phase tensor information. Figure 2a makes it clear why raw ellipses are a problem when one of the principal phases has a large range. It also shows the utility of plotting induction arrows concentric with the ellipses. Note that it is important to include some indication of the ellipse scale. It is common to rescale the ellipses so that all the major axes are equal and then fill the ellipses with a color indicating one of the principal phases. Which phase is used for the fill depends on what you want to emphasize. To accentuate the visual effect of large rotations of the ellipses as might occur crossing faults, minimum or maximum the principal phase can be used. Minimum phase is the most common. A very pretty example for the Taupo Volcanic Zone on the North Island of New Zealand (Bertrand et al. 2012) using minimum phase on top of related information is shown in Fig. 3. To suppress color changes that involve only ellipse rotation, one can use the phase of the geometric mean of the principal values (i.e., phase tensor determinant phase; see Hill et al. 2009 for an example).
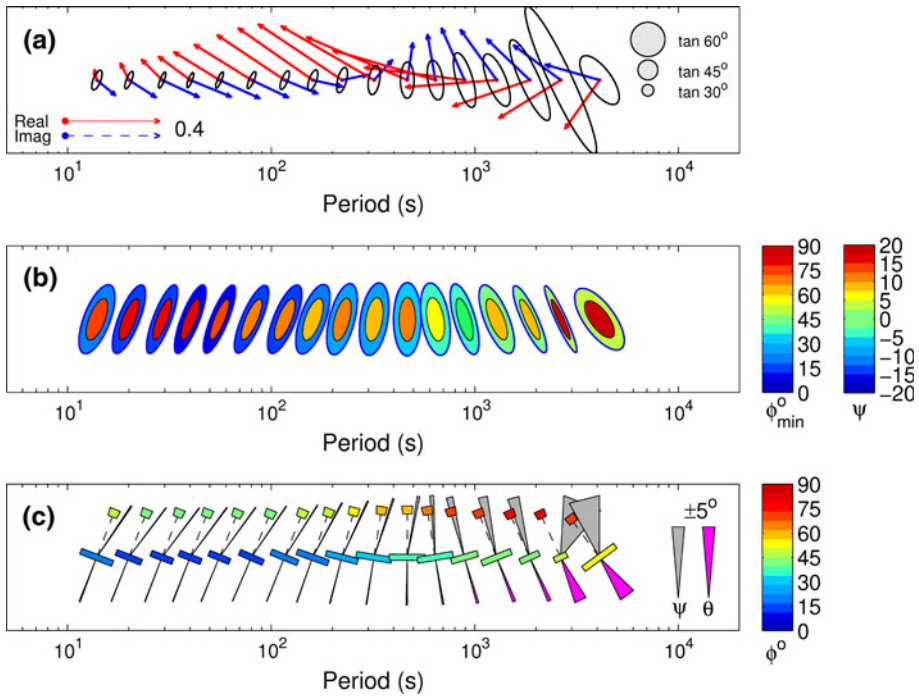
Fig. 2 Alternate ways of displaying phase tensor geometry at site pam885. **a** Unscaled ellipses with real and imaginary Parkinson vectors. Axis length scales for three phase angles are to the right. **b** Ellipses scaled so that all major axes are the same length. The outer ellipses are filled with color indicating the minimum principal phase. They surround ellipses with normalized skew angle fill color. **c** Scaled ellipse crosses with normalized skew angles. The skew angles and the downward pointing major axes are shown with uncertainty fans (*gray* is ψ and *magenta* is θ). Uncertainty fans with $\pm 5°$ are to the right for scale. The color of the ellipse minor axis indicates the minimum principal phase. The box at the end of the major axis is $\pm 6°$ wide. Its color indicates the maximum principal phase. For quasi-2D, the skew angle fan should overlap this box

The distribution of phase tensor skew angle is important in deciding whether 2D or 3D interpretation is required. Adding a concentric ellipse with color fill to indicate ψ as suggested by Ichihara et al. (2009) and shown in Fig. 2b is one way to simultaneously present the ellipse scale and skew angle information. At this site, the normalized skew appears too large to be consistent with 2D, but one cannot be certain without an estimate of the uncertainty. Simple maps and histograms of skew angle and ellipse axis direction like Fig. 4 are useful when the site density is too large to plot individual ellipses and clearly demonstrate the need for 3D interpretation in the case shown.

Figure 2c attempts to include the uncertainties of the axes directions and the normalized skew angle. Häuserer and Junge (2011) introduced ellipse axes "crosses" that were scaled to make the major axes constant and then colored so as to indicate both the maximum and minimum principal phase. Building on the idea of Xiao et al. (2010, 2011) to plot skew angles as lines rotated from the ellipse major axes, I have added error "fans" of the skew angle and the major axis direction to the crosses. A box at the end of the semi-axis closest to north is $\pm 6°$ wide. To be compatible with 2D, the skew angle fan must overlap this box. Now, it is clear that the normalized skew angle for this site is too large to be compatible
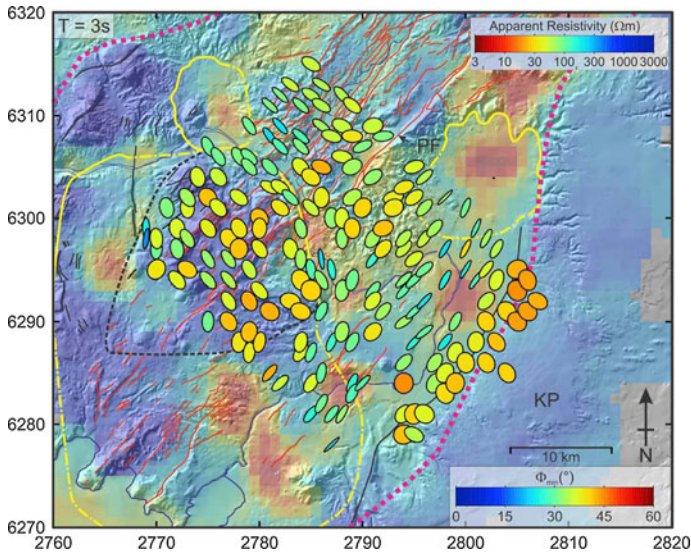
Fig. 3 Phase tensor ellipses at 3-s period scaled with major axes constant for an array of sites in the Taupo Volcanic Zone of New Zealand. The map scale is km on the New Zealand Map Grid. The color fill is minimum principal phase and the map background colors are DC apparent resistivity draped on digital elevation. Low-apparent resistivities correlate with thermal areas. *Solid orange lines* are topographic margins—presumably, tectonic faults and the *dashed lines* are inferred volcanic collapse faults. Modified from Bertrand et al. (2012)

with a quasi-2D interpretation at periods below 800 s and is marginally consistent at longer periods.

Two common problems in papers using color for skew angle when the goal is to justify quasi-2D interpretation are showing too wide a range of skew angles and too weak a gradation of colors. Together, these make it extremely difficult to judge whether $|\psi| \leq 6°$ (i.e., $|\beta| \leq 3°$). The otherwise very good examples by Thiel et al. (2009) and Yamaguchi et al. (2010) using pseudosections of skew angle to determine what part of the data should be interpreted using 2D suffer from this problem. The same is true for ellipse color fill showing skew angle in the paper by Schaefer et al. (2011). I recommend that the full-scale range of ψ be no more than $\pm 20°$ ($\pm 10°$ for β) and avoid continuous color or gray scales. In Fig. 2, there are very distinct color changes at 2.5° increments of ψ. The same color (green) is used for the range $-2.5° \leq \psi \leq +2.5°$ because these are values where consistency of a quasi-2D interpretation is in little doubt and green is the "go-ahead" color. With a gray scale, white can be substituted for green, but the quantized gradations of gray need to be large enough to be easily distinguished.

Finally, results that one may need to show are unusual circulation about the ellipse and the starting point for the ellipse circulation. As discussed in Appendix section "Principal Phase Signs," these are sufficient to determine the signs of the principal values. In Fig. 2c, one could eliminate one of the short semi-axis arms when the starting point has been reflected across the ellipse and the box around the short axis could be dashed when the circulation is counter to the unit circle. Plotting only 270° of the ellipse perimeter and making its perimeter dashed can convey the same information for standard ellipses.

Visualizing the distribution of phase tensor axes directions for many sites is almost always done using a rose histogram. Figure 5 shows two examples from Wannamaker et al.
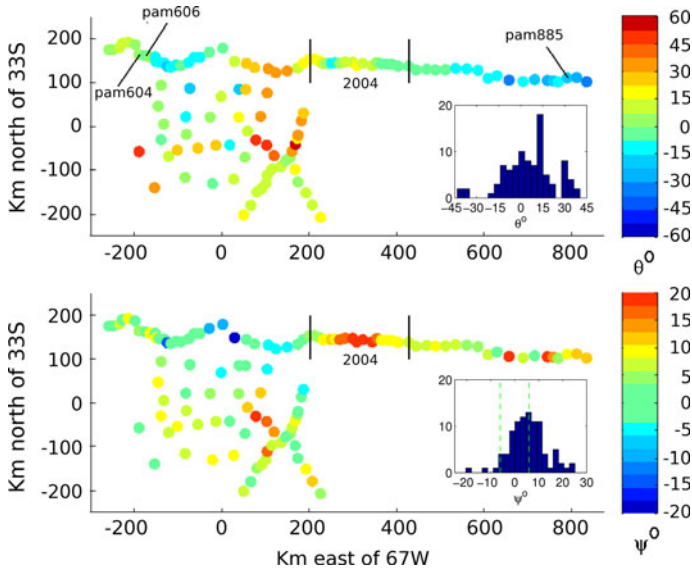
Fig. 4 Phase tensor ellipse axis directions (*top*) and normalized skew angles (*bottom*) at 1,280 s for an MT array in central Argentina. This period penetrates more than 200 km because the crust is crystalline with thin sedimentary cover. The uncertainties are much smaller than the variability. The sites bracketed by short vertical lines and labeled "2004" were used by Booker et al. (2004). The histograms exclude the 18 sites east of the 2004 profile. The north–south strike used by Booker et al. is supported by the mean θ of 4.3° for their sites and the broad histogram peak centered at 0° when all the sites to the west are also included. However, only 2 of their 18 sites have |ψ| ≤ 6° and 10 have |ψ| > 10°. Thus, the 2D assumption of Booker et al. is clearly problematic. The *dashed green lines* on the ψ histogram are at ± 6°. Only 47 of the 93 sites lie in this range and 22 have |ψ| > 10°. Booker et al. and a new 3D study by Burd et al. (2013) both find deep-sourced vertical current flow where the Nazca slab rolls over from flat subduction. The 2D study concludes the conductive channel is coincident with or just east of the plunging slab, while the 3D study finds a cylindrical conductor that pierces any reasonable extrapolation of the slab deeper than 200 km. The tectonic implications of the two models are very different. MT sites used elsewhere in this paper are also shown (see Appendix 2.4 for further details)

(2008) and Unsworth et al. (2007). The diagrams of Wannamaker et al. are commendable because they include uncertainties of the averages based on a statistical analysis of the direction distribution. Most papers take no notice of the uncertainties involved.

2.5 Data Quality

The simplest application of the phase tensor is monitoring data quality. Smooth variation of the phase tensor with period and position is a strong indicator of data consistency. The next to longest period in Fig. 2c is much larger than the prior periods as is its error. This is a certain indicator of deteriorating data. In his latest robust time series processing code, Jimmy Larsen (personal communication) uses the phase tensor to verify consistency of response estimations where processing bands overlap. Bertrand et al. (2012) also discuss using the spatial coherence of the phase tensor as a requirement for high-quality data. This coherence is evident in Figs. 3 and 4.
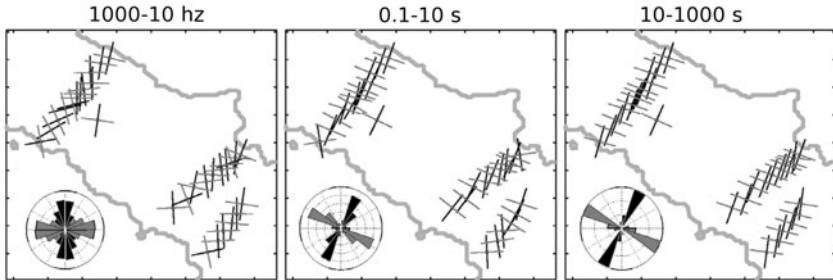
(a) Great Basin Profile
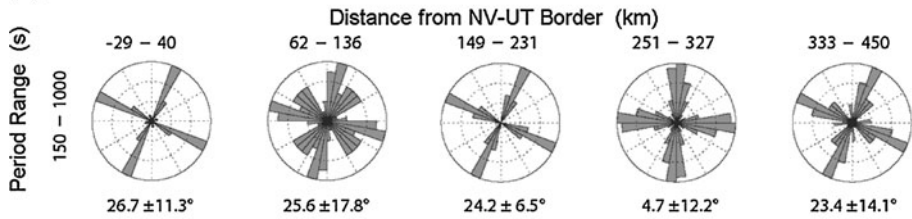
Fig. 5 **a** Rose histogram of phase tensor ellipse axes in the 150–1,000 s bandwidth for five segments of an east–west profile in Nevada and Utah. The standard deviations of the most probable strikes are based on the statistics of circular distributions. This figure is based on Wannamaker et al. (2008) **b** Rose histograms and individual site crosses for three period ranges along 3 profiles across Amchitka Island in the Aleutian Islands of Alaska. The maps are 9.5 km on a side. The site crosses are colinear with the phase tensor axes averaged over each sub-band but are not scaled to reflect principal phase values. The much larger variability in the shortest period band reflects the heterogeneity of the very shallow structure. Based on Unsworth et al. (2007)

3 Phase Tensor Alternatives and Relatives

3.1 Induction Vectors

The vertical component of the magnetic field is commonly also measured and its relation to the horizontal magnetic field is modeled by

$$H_z = \mathbf{W}^T\mathbf{H} = \begin{bmatrix} W_x & W_y \end{bmatrix} \begin{bmatrix} H_x \\ H_y \end{bmatrix} \tag{25}$$

$\mathbf{W}$ is another complex transfer function commonly called the induction vector. It is also often called the "tipper" (cryptic jargon with no useful meaning). Like the impedance, $\mathbf{W}$ is assumed to be a stable property of Earth's interior. The statistical estimation issues are more difficult than for $\mathbf{Z}$ because H_z with a relation to local horizontal magnetic field identical to (25) can be generated by currents flowing above Earth's surface. I assume that these problems have already been addressed in the time series processing and can be ignored.

$\mathbf{W}$ is usually separated into its real and imaginary parts which are plotted as separate vectors on maps or pseudosections. When structure is 2D, these vectors are parallel and in the "Wiese" convention point away from electric current concentrations and thus perpendicular to strike. The sign of $\mathbf{W}$ is often reversed so that "Parkinson" vectors point toward the current.

Deviation from colinearity between the real and imaginary vectors is a simple measure of departure from 2D structure. Plotting them with their origins coinciding with the centers of phase tensor ellipses as in Fig. 2a is an often-used way of presenting their complementary information about structure directionality and dimensionality. Physically, the induction vector is the direction of the horizontal magnetic field that maximizes the vertical magnetic field, which in turn measures the induced current. As noted earlier, one of the axes of the phase tensor ellipse is also expected to be the direction of maximum induction. So the induction vectors and an ellipse will be colinear for 2D and should remain colinear for moderately 3D structure.

However, in general, the induction vector and the phase tensor do not see structural dimensionality in the same way because spatial distribution of electric current density that determines $\mathbf{W}$ does not have a one-to-one correspondence to the phase of the electric and magnetic fields that determine $\mathbf{\Phi}$. In Fig. 2a, periods shorter than 100 s have real and imaginary induction vectors closely colinear with the short ellipse axes. If one looks only at the phase tensor ellipses and does not know from Fig. 2c that ψ is too large even when its uncertainty is take into account, one might easily conclude that these data are compatible with shallow 2D structure whose strike is north-northeast–south-southwest with the lower phase corresponding to the TE mode. As period increases, the ellipses and induction vectors rotate smoothly counterclockwise. The real induction vector remains along the short ellipse axis, but the imaginary vector rotates more rapidly and ends up perpendicular to the real vector and thus parallel to the long ellipse axis from 450 to 1,250 s. The normalized skew angle is decreasing and its uncertainty is increasing so that, as I have already noted, it becomes marginally compatible with quasi-2D at the same periods. Thus, if one discounts the direction of the imaginary vector, one is tempted to conclude that deeper structure is still approximately 2D albeit with a somewhat different strike than the shallow structure. In actuality, this site is responding to a strongly 3D structure: a sharp change in direction of the edge of conductive Paraná Basin sedimentary rocks overlying a very resistive basement near the Uruguay River that forms the boundary between Argentina and Uruguay. The 3D nature of the response at all periods is clear only if all the phase tensor and induction vector information are considered.

One can summarize the literature of field applications of induction vectors together with phase tensors by saying that, when faced with conflicting information from multiple views of the structure dimensionality and strike, authors discount the information that does not support what they want to assume—usually that they can use a 2D interpretation. It is hoped that the increasing access to 3D interpretation tools will change this.

Because the induction vector does not involve the electric field directly, it is not subject to the same static distortion as $\mathbf{Z}$. However, it can be distorted in a related way because deflection of electric currents by in-phase electric fields can alter the vertical magnetic field even when the distortion of the horizontal magnetic field is negligible. This is sometimes called "current channeling" (e.g., Zhang et al. 1993; Jiracek 1990) and is discussed further in the next section.

3.2 The Enhanced Admittance Phase Tensor

Relation (1) can be inverted and, if the horizontal magnetic field $\mathbf{H}$ is undistorted, one can write

$$\mathbf{H} = \mathbf{AE} = \mathbf{A}_D \mathbf{E}_D = \mathbf{A}_D \mathbf{DE} \tag{26}$$

where $\mathbf{A}$ is called the regional "admittance tensor." $\mathbf{D}$ is again the distortion matrix and the subscripts D denote distorted quantities we actually observe. From (26), we obviously have

$$\mathbf{A} = \mathbf{A}_D \mathbf{D} \tag{27}$$

Letting the real and imaginary parts of $\mathbf{A}$ be $\mathbf{U}$ and $\mathbf{V}$, one can define an admittance phase tensor and use (27) to show that it is unaffected by distortion:

$$\mathbf{\Psi} = \mathbf{V}\mathbf{U}^{-1} = \mathbf{V}_D\mathbf{D}(\mathbf{U}_D\mathbf{D})^{-1} = \mathbf{V}_D\mathbf{D}\mathbf{D}^{-1}\mathbf{U}_D^{-1} = \mathbf{V}_D\mathbf{U}_D^{-1} = \mathbf{\Psi}_D \tag{28}$$

It is not difficult to prove that $\mathbf{\Psi} = -\mathbf{\Phi}$ which is the tensor equivalent of reversing the sign of the phase when the impedance is inverted. Thus, all the properties of the impedance phase tensor carry over trivially to this admittance phase tensor and it would seem we have gained nothing.

However, (26) can be enhanced to include the induction vector $\mathbf{W}$

$$\begin{bmatrix} \mathbf{H} \\ H_z \end{bmatrix} = \begin{bmatrix} \mathbf{H} \\ \mathbf{W}^T\mathbf{H} \end{bmatrix} = \begin{bmatrix} \mathbf{A} \\ \mathbf{W}^T\mathbf{A} \end{bmatrix}\mathbf{E} = \begin{bmatrix} \mathbf{A}_D \\ \mathbf{W}^T\mathbf{A}_D \end{bmatrix}\mathbf{E}_D = \begin{bmatrix} \mathbf{A}_D \\ \mathbf{W}^T\mathbf{A}_D \end{bmatrix}\mathbf{D}\mathbf{E} \tag{29}$$

from which one can see that the H_z is subject to static distortion. The enhanced admittance and its distorted equivalent are then defined by

$$\tilde{\mathbf{A}} \equiv \begin{bmatrix} \mathbf{A} \\ \mathbf{W}^T\mathbf{A} \end{bmatrix} = \begin{bmatrix} \mathbf{A}_D \\ \mathbf{W}^T\mathbf{A}_D \end{bmatrix}\mathbf{D} \equiv \tilde{\mathbf{A}}_D\mathbf{D} \tag{30}$$

Note that $\tilde{\mathbf{A}}$ has three rows and two columns. An enhanced admittance phase tensor $\tilde{\mathbf{\Psi}}$ which has the same shape as $\tilde{\mathbf{A}}$ and is immune to static distortion can be defined by post-multiplying its imaginary part by the inverse of the real part of $\mathbf{A}$ (i.e., $\mathbf{U}$) giving

$$\begin{aligned} \tilde{\mathbf{\Psi}} &= \mathrm{Im}(\tilde{\mathbf{A}})\,(\mathrm{Re}(\mathbf{A}))^{-1} = \mathrm{Im}(\tilde{\mathbf{A}})\mathbf{U}^{-1} = \mathrm{Im}\left(\tilde{\mathbf{A}}_D\mathbf{D}\right)(\mathbf{U}_D\mathbf{D})^{-1} \\ &= \mathrm{Im}(\tilde{\mathbf{A}}_D)\mathbf{D}\mathbf{D}^{-1}\mathbf{U}_D^{-1} = \mathrm{Im}(\tilde{\mathbf{A}}_D)\mathbf{U}_D^{-1} = \tilde{\mathbf{\Psi}}_D \end{aligned} \tag{31}$$

Expanding (31) using (30), the enhanced admittance phase tensor can finally be written using only measured quantities that may be statically distorted.

$$\begin{aligned} \tilde{\mathbf{\Psi}} &= \begin{bmatrix} \tilde{\Psi}_{xx} & \tilde{\Psi}_{xy} \\ \tilde{\Psi}_{yx} & \tilde{\Psi}_{yy} \\ \tilde{\Psi}_{zx} & \tilde{\Psi}_{zy} \end{bmatrix} = \mathrm{Im}(\tilde{\mathbf{A}}_D)\,\mathbf{U}_D^{-1} = \mathrm{Im}\begin{bmatrix} \mathbf{A}_D \\ \mathbf{W}^T\mathbf{A}_D \end{bmatrix}\mathbf{U}_D^{-1} \\ &= \begin{bmatrix} \mathbf{V}_D \\ \mathrm{Im}(\mathbf{W}^T\mathbf{A}_D) \end{bmatrix}\mathbf{U}_D^{-1} = \begin{bmatrix} \mathbf{\Psi} \\ \mathrm{Im}(\mathbf{W}^T\mathbf{A}_D)\,\mathbf{U}_D^{-1} \end{bmatrix} = \begin{bmatrix} -\mathbf{\Phi} \\ \mathbf{T} \end{bmatrix} \end{aligned} \tag{32}$$

where I have introduced the distortion-free vertical field "phase vector"

$$\mathbf{T} = \mathrm{Im}(\mathbf{W}^T\mathbf{A}_D)\,(\mathrm{Re}(\mathbf{A}_D))^{-1} \tag{33}$$

The admittance phase tensor was first proposed in the context of a 3D inversion by Koyama (2009). The enhanced phase tensor is due to Pankratov and Kuvshinov (2010) who provide formulas for computing the partial derivatives of $\tilde{\mathbf{\Psi}}$ with respect to a 3D conductivity model. Applications of the geometry of the undistorted H_z phase vector $\mathbf{T}$ are likely to prove a useful complement to the phase tensor geometry, but have not yet been investigated.

3.3 The Conjugate Impedance Transform

Cai et al. (2010) propose another function of the MT impedance that is free of static distortion:

$$\mathbf{\Theta} = \mathbf{Z}^{-1}\mathbf{Z}^* \tag{34}$$

where * denotes complex conjugation. Their notation has been changed from Z_t to $\mathbf{\Theta}$ to avoid confusing it with impedance. It is in fact a phase tensor. I have not examined whether it has any advantages over the Caldwell et al. phase tensor.

3.4 Mohr Circles

A series of papers (Lilley 1998a, b; Weaver and Lilley 2004; Marti et al. 2005; Weaver et al. 2006; Martí et al. 2010 and Lilley 2012) have studied invariants of the MT impedance that can be used to constrain the dimensionality and directionality of subsurface structure. The Mohr circle is used to present this information in a compact geometrical form. A full discussion is beyond the scope of this review because these invariants are subject to static distortion except for a subset that is completely equivalent to the phase tensor parameters (Weaver and Lilley 2004, Weaver et al. 2006; Lilley 2012). Furthermore, I find the Mohr circle too complex to easily use in the context of a large number of sites and many periods, although Lilley and Weaver (2010) show how to present multiple periods in a useful format. It is best used for impedances at individual sites with complexities that are not understood after looking at the phase tensor.
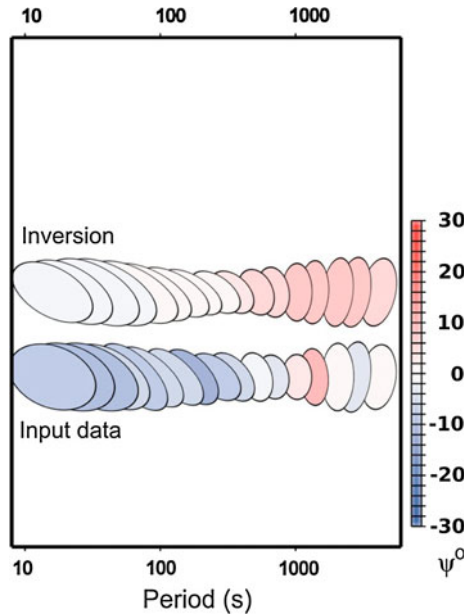
4 Inversion of the Phase Tensor

4.1 One- and Two-Dimensional Inversion

When the structure is 2D or quasi-2D, the principal phases immediately give the undistorted phases of the TM and TE mode impedances in the strike coordinates. It is therefore remarkable that I found no published example where principal phase data (or their values corrected for nonzero ψ as discussed in connection with parameterization (23)) are inverted for 2D structure.

The only published example of inversion of principal phases is by Roux et al. (2011). Building on the conclusion of Gatzemeier and Moorkamp (2005) that MT data in Central Germany are consistent with electrical anisotropy that varies primarily with depth, Roux et al. jointly invert Rayleigh wave dispersion curves and split phase tensor principal phases at a single site using a 1D anisotropic genetic algorithm. They conclude that there are two electrically anisotropic layers whose anisotropy directions differ. The anisotropy azimuth of the crustal layer is constrained only by the MT data while that of the deeper layer is constrained by the azimuth of the Rayleigh wave anisotropy. Phase tensor ellipses and skews for the measurements and one of their MT models are shown in Fig. 6. The principal phases appear well fit if the error bars, which are not shown, can be reliably estimated from the scatter. However, the measured data have large negative skew angles at short periods and small skew angles at long periods while the predicted skew angles are small at short period and large and positive at long period. As discussed above, the skew is arguably at least as important as the phase split when anisotropy direction varies with depth and this

Fig. 6 Observed and predicted phase tensor ellipses for a site in central Germany (modified from Roux et al. 2011). The inversion is 1D with anisotropy that varies with depth. The ellipse sizes and orientations match well. However, the observations have large skew magnitudes at short period and small at long period. The inversion has the opposite. In 1D, skew can only be generated by depth dependence of the anisotropy direction. The large discrepancy in skew magnitudes suggests that the model has incorrect depth dependence of the anisotropy azimuth

discrepancy implies that the depth dependence of the anisotropy direction is probably incorrect. Skew should have been included in the inversion.

4.2 Three-Dimensional Inversion

The phase tensor is a statically undistorted 3D response and as such deserves to be directly inverted by 3D algorithms. Before this can happen, however, it is necessary to compute the derivatives (sensitivities) of phase tensor parameters with respect to 3D model structure and devise optimum ways to constrain the absolute resistivity scale that is missing from the phase tensor.

Pankratov and Kuvshinov (2010) provide derivatives for the enhanced admittance phase tensor discussed earlier and demonstrate that their computation should be as efficient as computing derivatives of the impedance tensor elements. Egbert and Kelbert (2012) use an approach to the calculation of derivatives that differs from Pankratov and Kuvshinov primarily in discretizing the model from the outset. Neither of these papers presents a practical implementation.

Patro et al. (2012) have modified the "data space" code WSINV3DMT (Siripunvaraporn et al. 2005) to incorporate the phase tensor. They linearize the derivative of (3) with respect to the real and imaginary impedance elements and then use already computed sensitivities of the impedance elements with respect to the model. Inversions of the phase tensor alone, like 2D inversions of only impedance phase, are strongly affected by the details of the method that sets the absolute scale for the conductivities. The implementation of Patro et al. relies on the starting model to set this scale. Not surprisingly, this works well for data generated from a model essentially the same as used by Caldwell et al. (2004) contaminated with distortion when the starting half-space is the same as the original model background. It produces biased results when the starting model is too conductive or too

resistive. They also apply the same algorithm to the large USArray MT data set in the U.S. Pacific Northwest. The scale is determined by a 100 Ohm-m starting model plus a fixed Pacific Ocean. The results are presented after only two iterations but are sufficient to show that the inversion appears to be going in the right direction. A major issue that needs to be addressed is a more geologically conditioned way of constraining the overall scale. It would also be useful to find out whether inverting the parameterization (16) can be more effective than inverting the elements of the phase tensor in measurement coordinates. The reason is that data weighting based on data uncertainties and imposed error floors can then be controlled more easily to emphasize or de-emphasize the 3D aspects embodied in the normalized skew ψ.

4.3 Phase Tensor Misfit

Even if phase tensor data are not inverted, comparing predicted and observed phase tensors is an excellent way to assess modeling success. Heise et al. (2007) introduced the idea of a phase tensor misfit tensor defined by

$$\mathbf{\Delta} = \mathbf{I} - \frac{1}{2}\left(\hat{\mathbf{\Phi}}^{-1}\mathbf{\Phi} + \mathbf{\Phi}\hat{\mathbf{\Phi}}^{-1}\right) \tag{35}$$

(where the ^ signifies the phase tensor predicted by the model) as a way to judge whether 2D inversion is systematically unable to fit data influenced by 3D structure. Note that I have *interchanged the role of the observed and predicted phase tensor*s compared to the original definition of Heise et al. because the predicted tensor is not subject to noise and is a more stable quantity to invert. Figure 7 shows their pseudosection of $\mathbf{\Delta}$ ellipses. The regions of large ellipses clearly show where 2D inversion is probably inadequate. I say probably because issues such as data bias or 2D problems such as in incorrect choice of strike may also contribute.

Heise et al. (2008) extended these ideas to visualizing systematic misfit when the data, a forward modeling exercise and an inversion, are all 3D. Particularly interesting is their use of maps of $\mathbf{\Delta}$ ellipses to follow the progress of the inversion as iterations proceed.

However, the misfit tensor (35) has disadvantages. As shown in Appendix 2, it depends on the coordinate system in which it is evaluated. Second, if the residual between the predicted and measured skew angles is small, (35) simplifies to

$$\mathbf{\Delta} = \begin{bmatrix} \hat{\Phi}_a - \Phi_a/\hat{\Phi}_a & 0 \\ 0 & \hat{\Phi}_b - \Phi_b/\hat{\Phi}_b \end{bmatrix} \tag{36}$$

It is clear that the misfit ellipse shape depends on the phase magnitudes as well as the misfits and that the smallest principal phase dominates. This is why phase residuals used in inversions are always absolute phase differences which correspond to relative differences in impedance element magnitudes or, equivalently, absolute differences in log $\mathbf{Z}$. Therefore, I suggest that a more appropriate phase tensor misfit tensor is simply

$$\mathbf{\Delta}_{\text{absolute}} = \mathbf{\Phi} - \hat{\mathbf{\Phi}} = \mathbf{\Phi}_{\text{observed}} - \mathbf{\Phi}_{\text{predicted}} \tag{37}$$

which can be implemented as pseudosections and maps of the residuals of ψ, θ_{ellipse} and the principal phases or their phase split or as Heise et al. have done as color filled ellipses.
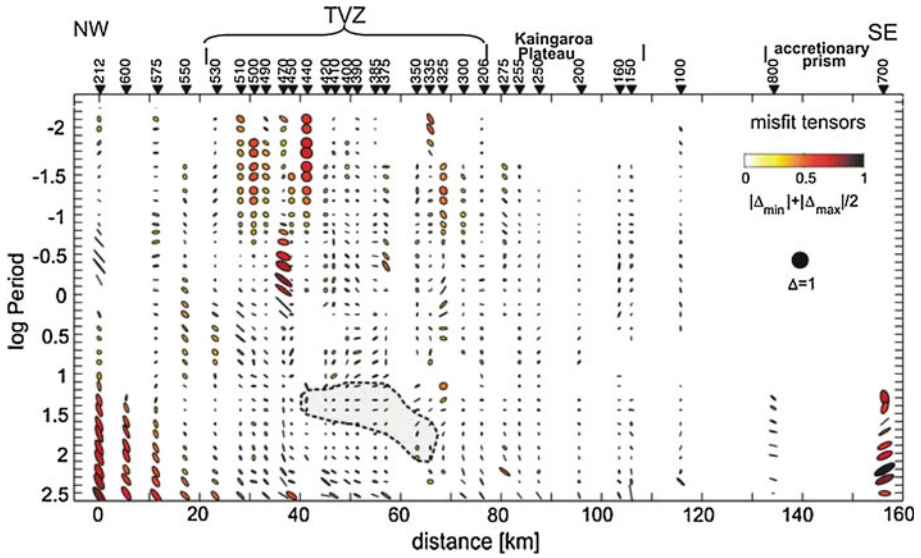
Fig. 7 An example of using the phase tensor misfit tensor $\mathbf{\Delta}$ to examine how well a 2D inversion fits data with 3D influences. Large ellipses signify poor misfit and hence failure of the 2D inversion to adequately characterize the 3D data. The long axis of the ellipse indicates which polarization is most poorly fit. The *dashed line* with *gray fill encircles* data that constrain a conductive zone between 10 and 20 km depth under the Taupo Volcanic Zone (TVZ) in New Zealand. The phase tensor predicted by the inversion matches the observed phase tensor very well in this gray region. The biggest systematic discrepancies between the 2D prediction and the 3D data are at long period at the NW end of the profile. Modified from Heise et al. (2007)

5 Impedance Tensor Decomposition

5.1 Two-Dimensional Decomposition

Considerable progress dealing with the underdetermined nature of relationship (6) (twelve unknowns with only eight data) has been made in the case that the regional structure is 2D (Bahr 1988; Groom and Bailey 1989; Smith 1995). The distorted, measured impedance can then modeled by the relationship

$$\mathbf{Z}_D^{\text{observed}} = \mathbf{R}_\theta^{-1}\mathbf{D}\mathbf{Z}^{2D}\mathbf{R}_\theta = \mathbf{R}_\theta^{-1}\begin{bmatrix} \cos(\alpha_x) & -\sin(\alpha_y) \\ \sin(\alpha_x) & \cos(\alpha_y) \end{bmatrix}\begin{bmatrix} 0 & s_x Z_{xy} \\ s_y Z_{yx} & 0 \end{bmatrix}\mathbf{R}_\theta \qquad (38)$$

where θ is the angle between the measurement coordinates and the strike of the regional 2D structure and $\mathbf{D}$ is in the form used by Smith (1995) where α_x and α_y are the angles through which the regional electric field components are rotated by the distortion and s_x and s_y are their amplification factors. If desired, the Groom-Bailey distortion parameters can be computed using

$$twist = \frac{1}{2}(\alpha_x + \alpha_y) \quad \text{and} \quad shear = \frac{1}{2}(\alpha_x - \alpha_y) \qquad (39)$$

Setting the complex diagonal elements of $\mathbf{Z}^{2D}$ to zero has removed four unknowns from (6) and it is also seen that $\mathbf{D}$ has only two determinable parameters. The other two multiply the impedance elements and cannot be separated from their magnitudes. The angle θ adds an unknown and the number of recoverable parameters becomes seven to be determined

from the eight data in the complex measured impedance. Adding the constraint implied by static distortion that α_x, α_y, and θ are period-independent and fitting multiple periods simultaneously increases the ratio of data to parameters. This can be made even more over-constrained by assuming that θ is the same at multiple sites fit simultaneously (McNeice and Jones 2001).

The fact that the magnitudes of Z_{xy} and Z_{yx} can be determined only within multiplicative constants s_x and s_y means that their logarithms have an offset called "static shift" that is not constrained by the measured impedance. The literature is full of techniques to constrain these shifts and they will not be considered further.

The model (38) is commonly called "impedance tensor decomposition" or simply decomposition. I will call it "2D decomposition" to distinguish it from alternates to be described.

5.2 An Inconvenient Fact

There is a fundamental problem with fitting the 2D decomposition model (38) to field data that are not generated by a strictly 2D regional structure. The normalized skew of 2D impedance is always zero. Multiplication by any real matrix $\mathbf{D}$ does not alter the phase tensor, and arbitrary rotation does not change its skew. Thus, model (38) always has $\psi = 0$, and assuming the misfit between the 2D decomposition predictions and the measurements is due to random noise is a false premise unless the observed impedance has ψ equal to zero within its uncertainty (i.e., regional impedance is 2D or quasi-2D). Then, solving the over-constrained problem presented by (38) using any variant of least squares always results in systematically incorrect (i.e., biased) estimates of strike θ and $s_x Z_{xy}$ and $s_y Z_{xy}$. Standard statistical arguments based on misfit of the predicted and measured data are not appropriate because the residuals cannot be zero for perfect data.

This issue was raised in the initial papers of Caldwell et al. but appears to have had almost no impact on the MT community. Of the 50 papers that use the phase tensor to justify 2D data interpretation, 17 simultaneously apply 2D decomposition. Only 6 of these try to show that the measured impedances are quasi-2D. One otherwise excellent paper uses $|\psi| \leq 8°$ ($|\beta| \leq 4°$) to exclude data from a phase tensor strike average but not from 2D decomposition (Pous et al. 2011). If one insists on using 2D decomposition, one should at least use the phase tensor skew angle to eliminate data for which this model is clearly invalid.

A reason put forward for adding horizontal magnetic distortion to the 2D decomposition was its failure to fit important aspects of the data. Since failure is guaranteed when phase tensor skew is not zero *even when the distortion is not magnetic*, I argue that one should first look at the phase tensor-consistent decompositions that follow before adding the complexity of horizontal magnetic field distortion discussed by Chave and Smith (1994).

5.3 Phase Tensor-Consistent Decomposition

There are many geological contexts in which regional structure is approximately 2D. Furthermore, when it is justified, impedance tensor decomposition extracts more information than the phase tensor. It is therefore clearly worth considering whether the original ideas of Bahr and Groom and Bailey can be re-formulated to be consistent with the phase tensor. The conceptual difficulty just discussed can be overcome using a generalization of 2D tensor decomposition: Instead of forcing the diagonal elements of the regional impedance to be zero, seek to make them as small as possible while still satisfying ψ. The

off-diagonal elements are then an estimate of quasi-2D impedance that is compatible with the phase tensor. How useful this estimate is depends on how big the diagonal elements are. Even if they turn out to be too large to ignore, the decomposed impedance is the 3D response that absorbs as much of its 3D nature into a real distortion matrix as possible.

The 2D decomposition model (38) is replaced with

$$
\begin{aligned}
\mathbf{Z}_D^{\text{observed}} &= \mathbf{R}_\theta^{-1} \mathbf{Z}_D \mathbf{R}_\theta = \mathbf{R}_\theta^{-1} \mathbf{D} \mathbf{Z}^{\text{regional}} \mathbf{R}_\theta \\
&= \mathbf{R}_\theta^{-1} \begin{bmatrix} \cos(\alpha_x) & -\sin(\alpha_y) \\ \sin(\alpha_x) & \cos(\alpha_y) \end{bmatrix} \begin{bmatrix} s_x Z_{xx} & s_x Z_{xy} \\ s_y Z_{yx} & s_y Z_{yy} \end{bmatrix}^{\text{regional}} \mathbf{R}_\theta
\end{aligned} \tag{40}
$$

plus the constraints

$$
Q_x = \left| \frac{Z_{xx}}{Z_{xy}} \right|^{\text{regional}} = \min \quad Q_y = \left| \frac{Z_{yy}}{Z_{yx}} \right|^{\text{regional}} = \min \tag{41}
$$

The static shift factors s_x and s_y are still not determinable separately from the magnitudes of the impedance elements they multiply. This model has 11 parameters to be determined by the 8 data plus 2 constraints. To close the problem, we need one more constraint. An obvious choice is to set

$$
\theta = \theta_{\text{ellipse}} \tag{42}
$$

We can then solve for all parameters exactly. Thus, (40) to (42) is actually a property of the measured impedance not a model. Because a real distortion matrix and rotation do not alter ψ, the regional and observed impedances in (40) have the same ψ.

The constraints (41) turn out to be surprisingly easy to implement. In Appendix 3, it is shown that

$$
\left| \frac{Z_{xx}}{Z_{xy}} \right| = Q_x = \left| \frac{Z_{Dxx} + Z_{Dyx} \tan(\alpha_y)}{Z_{Dxy} + Z_{Dyy} \tan(\alpha_y)} \right| \tag{43}
$$

and

$$
\left| \frac{Z_{yy}}{Z_{yx}} \right| = Q_y = \left| \frac{Z_{Dyy} - Z_{Dxy} \tan(\alpha_x)}{Z_{Dyx} - Z_{Dxx} \tan(\alpha_x)} \right| \tag{44}
$$

where $\mathbf{Z}_D$ is the observed impedance in ellipse coordinates. Thus, satisfying constraints (41) is a simple matter of rotating the observed impedance to ellipse coordinates and searching for the angles $\alpha_y^{\min}$ and $\alpha_x^{\min}$ that minimize the right sides of (43) and (44). These two searches are decoupled and involve only distorted impedance elements. They would be coupled and more difficult if the Groom-Bailey distortion parameters twist and shear were used.

Figure 8 shows 80-s period curves of $Q_x(\alpha_y)$ and $Q_y(\alpha_y)$ at site pam606 (see Appendix section "Site Locations and Data"). θ_{ellipse} is $5.09° \pm 0.24$. The normalized skew angle ψ is $9.68° \pm 0.32$ and thus too large for the phase tensor to be obviously quasi-2D. The minima associated with the optimum distortion angles are deep and narrow with

$$
\alpha_x^{\min} = -32.1° \pm 0.3 \quad Q_y\left(\alpha_x^{\min}\right) = 0.049 \quad \alpha_y^{\min} = 44.9° \pm 0.8 \quad Q_x\left(\alpha_y^{\min}\right) = 0.12
$$

The Groom-Bailey parameters are *twist* = $6.4°$ and *shear* = $-38.5°$. This impedance is strongly distorted, but Q_x and Q_y (the ratios of the undistorted diagonal to the off-diagonal
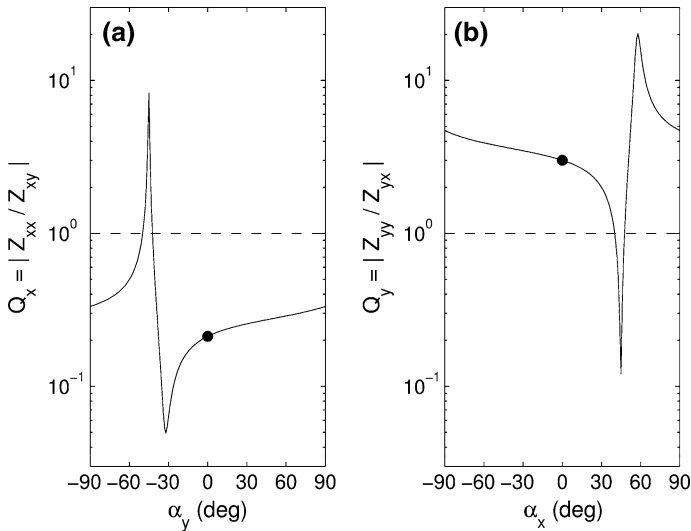
Fig. 8 Ratio of the diagonal to off-diagonal regional impedance elements as the distortion angles rotate through 180°. Each angle has a sharp minimum ratio of the diagonal to off-diagonal magnitudes that is much smaller than the ratio of the original magnitude (the dot at angle 0). Note that the optimum distortion angles are large

element magnitudes) are small enough that the quasi-2D assumption in which they are ignored appears quite reasonable.

Figure 9a and b plot phase tensor crosses, induction vectors, skew angles, and phase tensor distortion angles from 13 to 1,230 s at the same site. By typical standards, site pam606 appears 2D with a strike close to north–south. The induction vectors are mostly east–west and the major axes of the ellipses are nearly north–south. However, θ_{ellipse} rotates 30° across the bandwidth, the skew angle is not zero within its uncertainty at short periods, and, in Fig. 9c, the distortion angle α_y for the regional electric field perpendicular to θ_{ellipse} rotates significantly at longer periods.

The period dependence of α_y seems to imply failure of the assumption of static distortion. However, distortion angles computed in different coordinate systems cannot be directly compared. If the regional electric field rotates, the electric charges that distort it to produce the observed field also change and so do the distortion angles. Thus, period independence of distortion angles can only be tested if they are all computed in the same coordinate system. Consequently the observed period dependence of α_y may be due entirely to the period dependence of θ_{ellipse} and not to failure of the static distortion assumption.

To test this, constraint (42) can be replaced with the requirement that θ and the distortion angles do not depend on period. Specifically, seek an optimum θ_o that minimizes the mean-square misfit between the distortion angles and their period average. Figure 9d shows the result. The strike $\theta_0 = -10.4°$ makes **D** very close to the goal of period independence. We can conclude that the distortion is compatible with the static assumption over the full bandwidth.
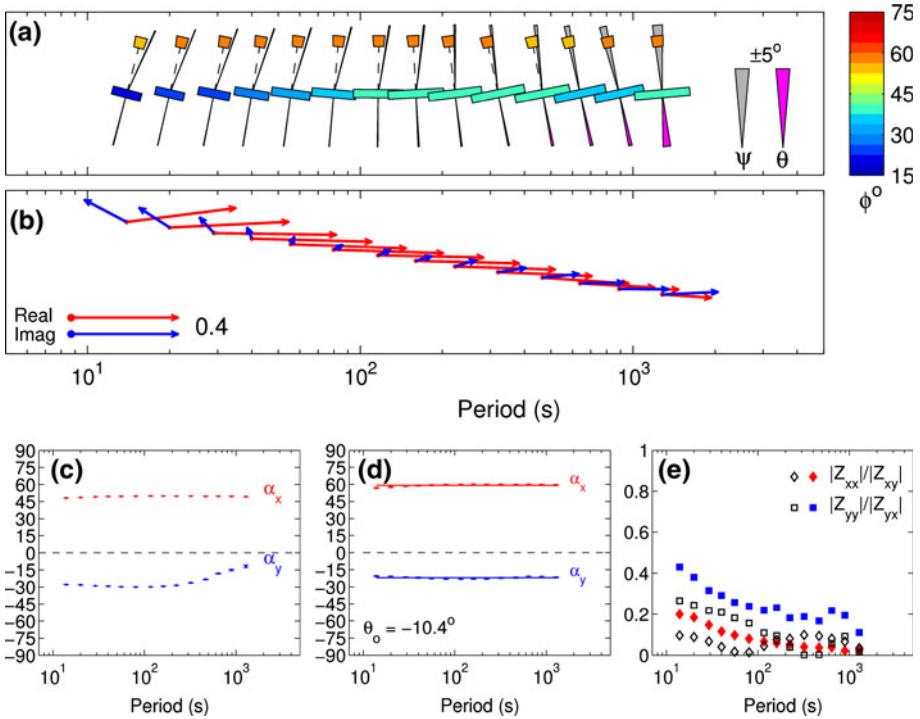
Fig. 9 a Phase tensor crosses for site pam606. See Fig. 2c for a detailed description of this type of presentation. **b** Real and imaginary Parkinson vectors with true north up. **c** Period-by-period phase tensor-consistent distortion angles in ellipse coordinates Note that x and y at each period are parallel and perpendicular to θ_{ellipse} which depends on period. The angles at 80 s are the same as in Fig. 8. **d** Phase tensor-consistent distortion angles in the coordinate system which minimizes their period dependence. **e** Ratios of the diagonal to off-diagonal magnitudes for the regional impedances in ellipse coordinates (*open symbols*) and in the optimum regional strike (*filled symbols*)

The undistorted impedance (within static shift factors) is recovered by inverting (40) to give

$$\mathbf{Z}^{\text{regional}} = \mathbf{D}^{-1}\mathbf{R}(\theta_0)\mathbf{Z}_D^{\text{observed}}\mathbf{R}^{-1}(\theta_0) \qquad (45)$$

This does not mean, however, that this regional impedance is quasi-2D, which depends on whether the diagonal elements are small enough to ignore. The ratios (43) and (44) of the diagonal to off-diagonal magnitudes for the undistorted impedances in both ellipse coordinates and the optimum period-independent strike are plotted in Fig. 9e. In general, but not always, there is an increase in the diagonal elements between ellipse and θ_0 coordinates. Z_{xx} appears small enough to ignore in both coordinate systems. However, at the shorter periods, Z_{yy} is almost certainly too large to ignore in the θ_0 system.

Note that θ_0 is needed only to compute the undistorted impedance. Once the undistorted regional impedance is known, it can be rotated to any coordinate system convenient for regional 3D interpretation. It can be rotated to other coordinates for quasi-2D interpretation in which one ignores the diagonal elements as long as the diagonal elements remain small enough. I leave further discussion of these results to a paper in preparation.

6 Concluding Remarks

This paper has revisited the basic theory of the magnetotelluric phase tensor. By developing its geometry in an intuitive way, I hope it becomes easier to apply to the important problems of ascertaining the dimensionality and directionality of MT data. When correctly used, which means not inflating the limits on skew angle and taking into account the uncertainties, the phase tensor will often lead to the conclusion that 2D interpretation is not justified for many data sets for which this assumption is presently being made. This should be considered an opportunity not an impediment to progress in this field because it will help prevent unwarranted conclusions and focus interpretation on three dimensionality when it is essential.

Appendix 1

Computing phase tensor parameters

All standard SVD algorithms easily compute the magnitudes of the tangents of the principal phase angles, but SVDs are not unique and so extracting an ellipse axis direction θ and determining the correct quadrant for the phases is a problem. A practical way to compute θ follows directly from the geometrical development above. With ω measured in the right-hand sense from the x-axis of the measurement coordinates, find the angle ω_0 such that either the vector

$$\mathbf{p}(\omega_0) = \mathbf{\Phi}\,\mathbf{c}(\omega_0 + \psi) \tag{46}$$

is parallel to the vector $\mathbf{c}(\omega_0 - \psi)$ or that

$$\left[\frac{\partial}{\partial\omega}|\mathbf{p}(\omega)|^2\right]_{\omega=\omega_0} = 0 \tag{47}$$

The first condition is probably easier to code in lower-level languages such as C or FORTRAN and should be more stable in nearly degenerate cases. The second is coded easily in high level languages such as Matlab that have built-in routines to find the zero of a function. Then, $\theta = \omega_0$ and the lengths of the semi-axes are

$$|\Phi_a| = \left|\mathbf{\Phi}_{\text{ellipse}}\mathbf{c}(\theta + \psi)\right| \tag{48}$$

$$|\Phi_b| = \left|\mathbf{\Phi}_{\text{ellipse}}\mathbf{c}(\theta + \psi + 90^\text{o})\right| \tag{49}$$

where $\mathbf{\Phi}_{\text{ellipse}}$ is computed using Eq. (15). The direction of circulation around the ellipse relative to the unit circle is determined by computing $\mathbf{p}(\omega)$ for two slightly increasing values of ω and seeing which direction the vector $\mathbf{p}$ rotates. Finally, determining the signs of Φ_a and Φ_b from the circulation of the ellipse is summarized in Table 2 in Section A.3.

Estimating Uncertainties

The phase tensor is a nonlinear function of the impedance, and the phase tensor decomposition parameters are nonlinear functions of the phase tensor. The situation is made worse by the fact that the phase tensor and derived parameters such as normalized skew are ratios of random variables. This can lead to distributions with formally infinite second moments. In a rigorous sense, the variance is then undefined (see Chave 2012b). This does not mean, however, that the uncertainties are unbounded or even that they are difficult to estimate. Statisticians have invented what is commonly called the "delta method" that is applicable to such situations (see Freedman, http://www.stat.berkeley.edu/∼census/ratest.pdf and Efron 1982, chapter 6). Operationally, it amounts to linear propagation of errors.

In the context of phase tensor parameters, the N-parameters by 4 complex matrix $\mathbf{J}$ of derivatives of the parameters with respect to the complex data are computed and then the N by N covariance of the parameters is given by

$$\boldsymbol{\Sigma}_{\text{parameters}} = \mathbf{J}\,\Sigma_{\text{obs}}\mathbf{J}^T \qquad (50)$$

where Σ_{obs} is the 4 by 4 complex covariance of the impedance (see Efron 1982, p43, eq 6.22 for the real case). The error estimates of the parameters are the square root of the diagonal of $\Sigma_{\text{parameters}}$. For most parameters, computing the derivatives is only practical numerically. The real and imaginary parts of the impedance elements are separately perturbed up and down by a small amount, and changes in the computed parameters are divided by twice the magnitude of the perturbation. Care is needed to detect and correct for parameter quadrant jumps between the positive and negative perturbations. The complex derivative is

$$\mathbf{J} = \mathbf{J}_{\text{real}} + i\mathbf{J}_{\text{imag}} \qquad (51)$$

Monte Carlo simulations can be used to verify the delta method results and illustrate the problems. I concentrate here on ψ because Jones (2012b, p265) singled it out for poor statistical performance. A very large number of realizations (10^4 is generally much too small; I use 10^6) are generated by adding random noise to the real and imaginary impedance elements using eight independent normal distributions. This generates circularly symmetric Gaussian noise in each complex element. The distributions are scaled so that their standard deviations equal the standard errors estimated from the observations. The parameters are calculated for each realization and their means and standard deviations are computed from all the realizations. It is important to point out that this does not simulate the effect of covariance and can only be compared to delta method results with the off-diagonals of Σ_{obs} set to zero.

Table 1 compares ψ and its uncertainties using the Monte Carlo and delta methods. For the highly distorted impedance used in Sect. 5.3 and ignoring the off-diagonal covariance, the error estimates are essentially identical with no significant bias. However, including the full covariance in the delta method decreases the error estimate by more than a factor of three!

Figure 10a is a Quantile–Quantile (Q–Q) plot of the ψ Monte Carlo realizations versus a normal distribution. Both distributions are normalized so that their means are 0 and their standard deviations are 1. The plot is constructed by sorting the realizations of ψ by size. Then, the number of points with values in fixed intervals are counted and plotted against the number expected for the normal distribution. If the points lie on a straight line with slope 1, the distributions are identical. They are clearly extremely close. Strictly speaking, angles like ψ should be compared to a "wrapped" Gaussian. However, even with a million points, the probability of one point outside of 4.5 standard deviations ($\pm 5°$) is too small for

any such points to exist. With such a small total angle spread, the wrapped and standard Gaussian are indistinguishable.

The situation is more complicated for data with larger errors. To simulate this, the estimated errors of the off-diagonal impedance phases are increased to 1.5° (10 % of their apparent resistivity or 5 % of their magnitude). The error estimates of the diagonal element magnitudes are set equal to the error estimate of the off-diagonal in the same row on the premise that the noise is from the electric field. The Monte Carlo estimate of the uncertainty in Table 1b is now much larger than the delta method ignoring the off-diagonal covariance. Comparison with the full covariance is not shown because I know of no consistent way to alter the off-diagonal covariance. To see what has happened, look at the histogram of the ψ realizations in Fig. 10b. There are secondary outlier peaks near $\pm$ 180°. These are due to realizations that have pushed ψ out of quadrant and produced a distribution that is clearly not a wrapped Gaussian. The poor performance of the "High Noise 3D" error simulation reported by Jones (2012b), Table 6.5a) may be the same problem. As noted in Sect. 2.2.3 and Fig. 11b of Appendix section "Principal Phase Signs," values of ψ near $\pm$ 180° have the same degree of three dimensionality as values near 0. Thus, for a moderately 3D impedance with ψ_{mean} about 10°, outliers near $\pm180°$ are much more likely than highly 3D values of ψ near $\pm90°$. A rigorous study of how this quadrant wrapping should be "unwound" is needed, but it is reasonable to suppress the influence of these "antipodal" outliers by simply "trimming" (i.e., dropping) angles outside of $\pm90°$. Doing so (see Table 1b) brings the "trimmed" Monte Carlo standard deviation into close agreement with the delta method. The bias is only 1 % of the error. To avoid spurious asymmetry in the ψ distribution, one can make the region of included data symmetric about the mean. This reduces the already negligible bias a bit and so is not worth the effort.

The large impact of the covariance in Table 1a is a common, but not general, situation. Table 1c also shows results for a site that has a larger normalized skew and is thus more 3D, but has less distortion ($\alpha_x = 23.8°$; $\alpha_y = -22.7°$). The effect of covariance is much

Table 1 The phase tensor skew angle ψ (deg) and its 1 standard deviation uncertainty at two MT sites using Monte Carlo (MC) with 10^6 realizations and Delta (Δ) methods

Method	Σ	ψ	$\delta\psi$
(a) Site Pam606 with observed impedance errors			
MC	Diagonal	9.684	1.092
Δ	Diagonal	9.685	1.092
Δ	Full	9.685	0.317
(b) Site Pam606 with 5 % |Z| errors (see text)			
MC	Diagonal	8.859	57.243
Δ	Diagonal	9.685	25.409
"Trimmed" MC (see text)	Diagonal	10.063	25.745
(c) Site Pam604 with observed impedance errors			
Δ	Diagonal	14.083	0.261
Δ	Full	14.083	0.207
(d) Site Pam604 with 5 % |Z| errors (see text)			
MC	Diagonal	14.080	6.585
Δ	Diagonal	14.089	6.525

Entries in the column headed Σ indicate whether the full covariance matrix or only its diagonal is used in the error estimate
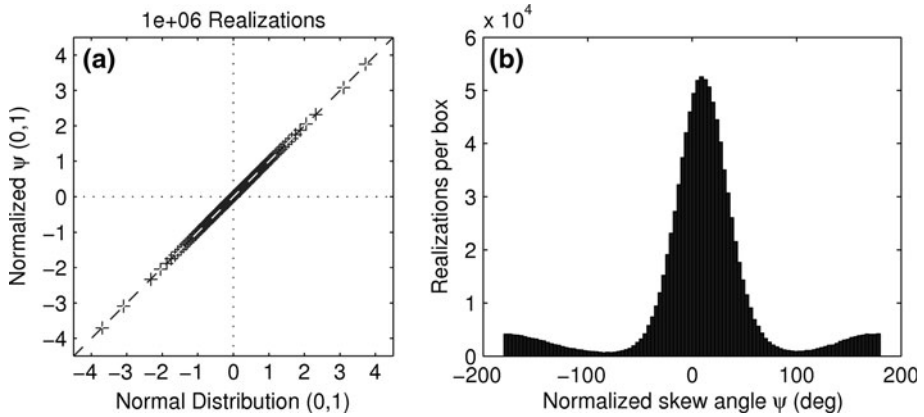
Fig. 10 **a** Q–Q plot of 10^6 random realizations of phase tensor skew angle ψ generated using observed impedance and error estimates at 80 s for site pam606. The realizations have been normalized so that they have zero mean and unit standard deviation. They are plotted against a normal distribution with the same mean and standard deviation. The axes units are standard deviations. If the ψ distribution is normal, the points should all fall on the straight line. **b** Histogram of 10^6 realizations of phase tensor normalized skew for the same impedance, but whose error estimates have been inflated as described in the text. The reason for the non-Gaussian secondary hump at $\pm180°$ and the justification for suppressing it are discussed in the text
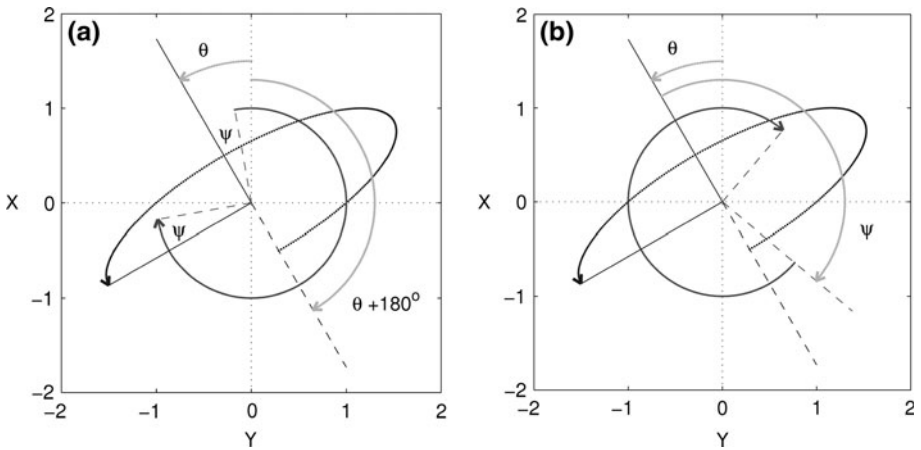

Fig. 11 Phase tensor ellipses with axes lengths and coordinate rotation identical to Fig. 1b. The normalized skew angle in (**a**) is the same as Fig. 1b, but the sign of the principal value Φ_a is negative and thus its principal phase is out of quadrant. Note that ellipse circulation is counter to that of the unit circle and that the ellipse starting point has moved to the opposite side of the origin. Note also that ψ is still measured from the original ellipse axis direction. This remains true when ψ is increased from 20 to 160° in (**b**)

smaller for this site. Inflating the errors at this second site by the same amount as in Table 1b leads to a ψ distribution with only 7 out of 10^6 antipodal values with essentially no impact on the Monte Carlo mean or error estimate (see Table 1d).

In my experience, large effects of covariance and strong distortion go together, but should never be assumed absent. Rotation always introduces covariance, and rotation of the variances alone will not in general give correct variances in the rotated frame. A rotation of 45° is the worst case. For example, ignoring the off-diagonals of the covariance at site pam604

(which is almost unaffected by covariance in Table 1(c)), the uncertainty at 80 s after a rotation of 45° is 32 % too small for $|Z_{xy}|$ and 34 % too large for $|Z_{yx}|$. Paraphrasing the title of Jones and Groom (1993): "rotate [ignoring covariance] at your peril." It is conceivable that their conclusions were actually the result of ignoring covariance.

One should not expect delta method uncertainties to be accurate for angles when the standard errors are greater than about ± 20° (4.5 standard deviations = 90°). Since angles with larger errors are of little use, this is not a practical problem. However, impedance covariance should never be ignored, especially for strongly distorted data. Computation of skew angle errors using a Monte Carlo method is clearly problematic. Not only must one identify and compensate for quadrant-flipped tails, but one cannot easily incorporate error covariance. Both can lead to grossly incorrect error estimates.

Principal Phase Signs

The sgn function is +1 when its argument is positive and −1 when its argument is negative. It can be used to rewrite (14) as

$$\mathbf{p}(\omega) = \begin{bmatrix} |\Phi_a| & 0 \\ 0 & |\Phi_b| \end{bmatrix} \mathbf{S}\,\mathbf{R}(\psi)\,\mathbf{c}(\omega) \tag{52}$$

where

$$\mathbf{S} = \begin{bmatrix} \mathrm{sgn}(\Phi_a) & 0 \\ 0 & \mathrm{sgn}(\Phi_b) \end{bmatrix} \tag{53}$$

is a "reflection" matrix. When Φ_a and Φ_b have opposite signs, this reflection reverses the circulation about the ellipse. Additionally, when $\Phi_a < 0$ and $\Phi_b > 0$, the starting point for the ellipse circulation moves to the opposite side of the origin. These relationships are summarized in Table 2 and examples are shown in Fig. 11. Plotting only 270° of the unit circle and ellipse and starting ω at $\theta + \psi$ (the semi-axis in the θ direction) makes it easy to see these relationships. Note that ψ is always measured from the "unreflected" semi-axis direction θ.

Site Locations and Data

The locations of the three MT sites used in this paper are shown in Fig. 4. They were collected in cooperation with Argentine colleagues. Site pam885 (31.724°S 58.627°W) used in Fig. 2 is in Entre Rios Province near the border between Argentina and Uruguay at the Uruguay River. It was collected using a Narod NIMS system sampling at 4 Hz. Site pam606 (31.531°S 68.839°W) is used in Figs. 8, 9, and 10 and in Table 1 is about 25 km

Table 2 Signs of phase tensor principal values as a function of circulation directions for the unit circle and phase tensor ellipse and ω_0, the starting angle of ellipse circulation

Unit circle	Ellipse	ω_0	Φ_a	Φ_b
Clockwise	Clockwise	$\theta_{\mathrm{ellipse}}$	+	+
Clockwise	Counterclockwise	$\theta_{\mathrm{ellipse}} + 180°$	−	+
Clockwise	Counterclockwise	$\theta_{\mathrm{ellipse}}$	+	−
Clockwise	Clockwise	$\theta_{\mathrm{ellipse}} + 180°$	−	−

west of the city of San Juan in a side valley of the San Juan River canyon in the Pre-Cordillera mountains of San Juan Province, Argentina. Site pam604 (31.509°S 68.999°W) also used in Table 1 is 15 km up the main canyon west of pam606. They were collected using LRMT systems (Phoenix clones of the Canadian Geological Survey LIMS) sampling at 5 s. All sites used lead–lead chloride electrodes separated by about 100 m. These data are available from a link at http://earthweb.ess.washington.edu/booker and will become available from the IRIS DMC (http://www.iris.edu/data/).

Appendix 2

The misfit tensor defined by Heise et al. (2007) is

$$\boldsymbol{\Delta} = \mathbf{I} - \frac{1}{2}\left(\hat{\boldsymbol{\Phi}}^{-1}\boldsymbol{\Phi} + \boldsymbol{\Phi}\hat{\boldsymbol{\Phi}}^{-1}\right) \tag{54}$$

(where the "hat" ^ signifies the phase tensor predicted by the model) with the exception that the role of the observed and predicted phase tensors have been interchanged. Rewriting $\boldsymbol{\Delta}$ using the rotationally invariant parameters of the phase tensor parameterization (16), we can show that (54) depends on the coordinate system in which it is computed.

$\boldsymbol{\Delta}$ is the average of "right-handed" and "left-handed" *relative misfits*

$$\boldsymbol{\Delta}_{\text{right}} = \left(\hat{\boldsymbol{\Phi}} - \boldsymbol{\Phi}\right)\boldsymbol{\Phi}^{-1} = \mathbf{I} - \boldsymbol{\Phi}\hat{\boldsymbol{\Phi}}^{-1} \tag{55}$$

$$\boldsymbol{\Delta}_{left} = \hat{\boldsymbol{\Phi}}^{-1}\left(\hat{\boldsymbol{\Phi}} - \boldsymbol{\Phi}\right) = \mathbf{I} - \hat{\boldsymbol{\Phi}}^{-1}\boldsymbol{\Phi} \tag{56}$$

It is now clear why interchanging the roles of the observed and model phase tensors is a good idea. The predicted phase tensor is not subject to random noise and makes a more stable quantity against which to compare the phase tensor principal values residual.

Choosing the coordinate system aligned with the predicted phase tensor, we can use the more compact notation

$$\hat{\boldsymbol{\Lambda}} \equiv \begin{bmatrix} \hat{\Phi}_a & 0 \\ 0 & \hat{\Phi}_b \end{bmatrix} \tag{57}$$

and (16) to write the predicted phase tensor

$$\hat{\boldsymbol{\Phi}} = \hat{\boldsymbol{\Lambda}}\mathbf{R}_{\hat{\psi}} \tag{58}$$

The observed phase tensor ellipse axes do not necessarily align with the predicted ellipse. Defining $\delta\theta$ as the angle of the observed ellipse axes to the predicted ellipse coordinate system, we can again use (16) to write the observed phase tensor in the predicted phase tensor coordinates

$$\boldsymbol{\Phi} = \mathbf{R}_{\delta\theta}\left(\boldsymbol{\Lambda}\mathbf{R}_{\psi}\right)\mathbf{R}_{\delta\theta}^{-1} = \left(\mathbf{R}_{\delta\theta}\boldsymbol{\Lambda}\mathbf{R}_{\delta\theta}^{-1}\right)\mathbf{R}_{\psi} \equiv \mathbf{L}\,\mathbf{R}_{\psi} \tag{59}$$

where $\mathbf{L}$ is the observed principal value matrix rotated to the predicted ellipse frame. Finally, in the predicted ellipse coordinate frame, the right-handed misfit tensor (55) becomes

$$\boldsymbol{\Delta}_{right} = \mathbf{I} - \mathbf{L}\,\mathbf{R}_{\delta\psi}\hat{\boldsymbol{\Lambda}}^{-1} \equiv \mathbf{I} - \tilde{\mathbf{L}}\,\hat{\boldsymbol{\Lambda}}^{-1} \tag{60}$$

where the skew angle residual $\delta\psi \equiv \psi - \hat{\psi}$ and

$$\tilde{\mathbf{L}} \equiv \mathbf{L}\mathbf{R}_{\delta\psi} = \mathbf{R}_{\delta\theta}\mathbf{\Lambda}\mathbf{R}_{\delta\theta-\delta\psi} \tag{61}$$

In the same coordinate frame, the left-handed misfit tensor (38) is

$$\mathbf{\Delta}_{left} = \mathbf{I} - \mathbf{R}_{\hat{\psi}}^{-1}\hat{\mathbf{\Lambda}}^{-1}\mathbf{L}\,\mathbf{R}_{\psi} \tag{62}$$

This can be simplified by rotating its coordinates by normalized skew angle $\hat{\psi}$ relative to the axes of the predicted ellipse and using the fact that $\hat{\mathbf{\Lambda}}$ is diagonal. The rotated misfit tensor is given the new name

$$\tilde{\mathbf{\Delta}}_{left} \equiv \mathbf{R}_{\hat{\psi}}\mathbf{\Delta}_{left}\mathbf{R}_{\hat{\psi}}^{-1} = \mathbf{I} - \hat{\mathbf{\Lambda}}^{-1}\mathbf{L}\,\mathbf{R}_{\delta\psi} = \mathbf{I} - \hat{\mathbf{\Lambda}}^{-1}\tilde{\mathbf{L}} = \mathbf{I} - \tilde{\mathbf{L}}^{\mathbf{T}}\hat{\mathbf{\Lambda}}^{-1} \tag{63}$$

The first thing to notice about (60) and (63) is that they differ only in the transpose of $\tilde{\mathbf{L}}$. Thus, $\mathbf{\Delta}_{\text{right}}$ and $\mathbf{\Delta}_{\text{left}}$ contain the same coordinate-invariant information. Averaging them confuses the situation because their difference is a consequence of the coordinate systems in which they are evaluated (which are rotated ψ relative to each other). If one wants to plot a phase tensor misfit tensor using relative residuals, it is better to choose one of the definitions (56), (57), (60) or (63), and not (54).

The second thing to notice is that, when the skew angle residual is small, the net rotation due to $\mathbf{R}_{\delta\psi}$ will be negligible even when ψ itself cannot be ignored. Thus, these misfit tensors are only weakly dependent on the magnitude of ψ and hence on the parameter that is unambiguously 3D. Better and far simpler ways of addressing how much a 2D or 3D inverse or model is violating 3D aspects of the data are pseudosections and maps of the normalized skew residual $\delta\psi$ and the angles $\delta\theta$ between the predicted and observed phase tensor ellipses.

Finally, if both $\delta\psi$ and $\delta\theta$ are negligible, (60) and (63) reduce to the result discussed earlier:

$$\mathbf{\Delta}_{\text{left}} = \mathbf{\Delta}_{\text{right}} = \mathbf{I} - \mathbf{\Lambda}\,\hat{\mathbf{\Lambda}}^{-1} = \begin{bmatrix} \hat{\Phi}_a - \Phi_a/\hat{\Phi}_a & 0 \\ 0 & \hat{\Phi}_b - \Phi_b/\hat{\Phi}_b \end{bmatrix} \tag{64}$$

Appendix 3

Smith (1995) showed that any static distortion matrix can be parameterized by

$$\mathbf{D} = \begin{bmatrix} a & c \\ b & d \end{bmatrix} = \begin{bmatrix} \cos(\alpha_x) & -\sin(\alpha_y) \\ \sin(\alpha_x) & \cos(\alpha_y) \end{bmatrix} \begin{bmatrix} g_x & 0 \\ 0 & g_y \end{bmatrix} \tag{65}$$

where

$$\tan(\alpha_x) = \frac{b}{a} \quad \tan(\alpha_y) = \frac{-c}{d} \quad g_x = \sqrt{a^2 + b^2} \quad g_y = \sqrt{c^2 + d^2} \tag{66}$$

"Distortion angle" α_x is the rotation and the "gain" factor g_x multiplies the magnitude of the x-component of the regional electric field; α_y is the rotation and g_y is the gain of the y-component of the regional electric field. It is then easy to show that the distorted regional impedance in regional coordinates can be expressed

$$\mathbf{Z}_D = \mathbf{DZ} = \begin{bmatrix} 1 & -\tan(\alpha_y) \\ \tan(\alpha_x) & 1 \end{bmatrix} \begin{bmatrix} \cos(\alpha_x)\,g_x Z_{xx} & \cos(\alpha_x)\,g_x Z_{xy} \\ \cos(\alpha_y)\,g_y Z_{yx} & \cos(\alpha_y) g_y Z_{yy} \end{bmatrix} \quad (67)$$

$$\equiv \tilde{\mathbf{D}}\tilde{\mathbf{Z}}$$

where $\tilde{\mathbf{D}}$ and $\tilde{\mathbf{Z}}$ are just rescaled versions of $\mathbf{D}$ and $\mathbf{Z}$.

Multiplying (67) by $\tilde{\mathbf{D}}^{-1}$ gives

$$\tilde{\mathbf{D}}^{-1}\mathbf{Z}_D = \frac{1}{\det(\tilde{\mathbf{D}})} \begin{bmatrix} 1 & \tan(\alpha_y) \\ -\tan(\alpha_x) & 1 \end{bmatrix} \begin{bmatrix} Z_{Dxx} & Z_{Dxy} \\ Z_{Dyx} & Z_{Dyy} \end{bmatrix}$$

$$= \frac{1}{\det(\tilde{\mathbf{D}})} \begin{bmatrix} Z_{Dxx} + Z_{Dyx}\tan(\alpha_y) & Z_{Dxy} + Z_{Dyy}\tan(\alpha_y) \\ -Z_{Dxx}\tan(\alpha_x) + Z_{Dyx} & -Z_{Dxy}\tan(\alpha_x) + Z_{Dyy} \end{bmatrix} \quad (68)$$

$$= \begin{bmatrix} \cos(\alpha_x)\,g_x Z_{xx} & \cos(\alpha_x)\,g_x Z_{xy} \\ \cos(\alpha_y)\,g_y Z_{yx} & \cos(\alpha_y) g_y Z_{yy} \end{bmatrix}$$

The magnitude of the ratio of the elements in the first row of (68) gives

$$\left| \frac{\cos(\alpha_x)\,g_x Z_{xx}}{\cos(\alpha_x)\,g_x Z_{xy}} \right| = \left| \frac{Z_{xx}}{Z_{xy}} \right| = Q_x = \left| \frac{Z_{Dxx} + Z_{Dyx}\tan(\alpha_y)}{Z_{Dxy} + Z_{Dyy}\tan(\alpha_y)} \right| \quad (69)$$

The magnitude of the ratio of the elements in the second row of (68) gives

$$\left| \frac{\cos(\alpha_y)\,g_y Z_{yy}}{\cos(\alpha_y)\,g_y Z_{yx}} \right| = \left| \frac{Z_{yy}}{Z_{yx}} \right| = Q_y = \left| \frac{Z_{Dyy} - Z_{Dxy}\tan(\alpha_x)}{Z_{Dyy} - Z_{Dyx}\tan(\alpha_x)} \right| \quad (70)$$

Thus, satisfying constraints (42) is a simple matter of searching for the angles $\alpha_y^{\min}$ and $\alpha_x^{\min}$ that minimize the terms on the right of (69) and (70).

References

Bahr K (1988) Interpretation of the magnetotelluric impedance tensor: regional induction and local telluric distortion. J Geophys (Z. Geophys.) 62(2): 119–127

Bertrand EA, Caldwell TG, Hill GJ, Wallin EL, Bennie SL, Cozens N, Onacha SA, Ryan GA, Walter C, Zaino A, Wameyo P (2012) Magnetotelluric imaging of upper-crustal convection plumes beneath the Taupo Volcanic Zone, New Zealand. Geophys Res Lett 39:L02304. doi:10.1029/2011GL050177

Bibby HM, Caldwell TG, Brown C (2005) Determinable and non-determinable parameters of galvanic distortion in magnetotellurics. Geophys J Int 163:915–930

Booker JR, Favetto A, Pomposiello MC (2004) Low electrical resistivity associated with plunging of the Nazca flat slab beneath Argentina. Nature 429:399–403. doi:10.1038/nature02565

Burd A, Booker J, Mackie R, Pomposiello C, Favetto A (2013) Electrical conductivity of the pampean shallow subduction region of Argentina near 33–S: evidence for a slab window. Geochem Geophys Geosyst Submitted MS 2013GC004732

Cai J-T, Chen X-B, Zhao G-Z (2010) Refined techniques for data processing and two-dimensional inversion in magnetotelluric I: Tensor decomposition and dimensionality analysis. Chinese J Geophys Chinese Ed. 53:2516–2526

Caldwell TG, Bibby HM, Caldwell C (2004) The magnetotelluric phase tensor. Geophys J Int 158:457–469

Caldwell TG, Bibby HM, Caldwell C (2007) Comment on "The magnetotelluric phase tensor" by T.Grant Caldwell, Hugh M. Bibby and Colin Brown: reply. Geophys J Int 171:565–567

Chave AD (2012a) Estimation of the magnetotelluric response function. In: Chave AD, Jones AG (eds) The magnetotelluric method theory and practice. Cambridge University Press

Chave AD (2012b) On the statistics of magnetotelluric skew. Geophys J Int (in review)

Chave AD, Smith JT (1994) On electric and magnetic galvanic distortion tensor decompositions. J Geophys Res Solid Earth 99:4669–4682

Chave AD, Thomson DJ (1989) Some comments on magnetotelluric response function estimation. J Geophys Res 94

Chave AD, Thomson DJ, Ander ME (1987) On the robust estimation of power spectra, coherences, and transfer functions. J Geophys Res 92:633–648

Efron B (1982) The Jackknife, the bootstrap and other resampling plans. CMMS-NSF Regional Conference Series in Applied Mathematics, SIAM doi: 10.101137/1.978161197039.ch6

Egbert GD (1997) Robust multiple-station magnetotelluric data processing. Geophys J Int 130:475–496. doi: 10.1111/j.1365-246X.1997.tb05663.x

Egbert G, Booker JR (1986) Robust estimation of geomagnetic transfer functions. Geophys J R Astr Soc 87:173–194

Egbert GD, Kelbert A (2012) Computational recipes for electromagnetic inverse problems. Geophys J Int 189:251–267

Freedman DA (2008) http://www.stat.berkeley.edu/~census/ratest.pdf

Gamble TD, Goubau WM, Clarke J (1979) Magnetotellurics with a remote reference. Geophysics 44:53–68

Gatzemeier A, Moorkamp M (2005) 3D modelling of electrical anisotropy from electromagnetic array data: hypothesis testing for different upper mantle conduction mechanisms. Phys Earth Planet Int 149:225–242

Groom RW, Bailey RC (1989) Decomposition of magnetotelluric impedance tensors in the presence of local three dimensional galvanic distortions. J Geophys Res 94:1913–1925

Groom RW, Bailey RC (1991) Analytical investigations of the effects of near surface three dimensional galvanic scatterers on MT tensor decomposition. Geophysics 56:496–518

Häuserer M, Junge A (2011) Electrical mantle anisotropy and crustal conductor: a 3-D conductivity model of the Rwenzori Regionin western Uganda. Geophys J Int 185:1235–1242

Heise W, Caldwell TG, Bibby HM, Brown C (2006) Anisotropy and phase splits in magnetotellurics. Phys Earth Planet Int 158:107–121

Heise W, Bibby HM, Caldwell G, Bannister SC, Ogawa Y, Takakura S, Uchida T (2007) Melt distribution beneath a young continental rift: the Taupo Volcanic Zone, New Zealand. Geophys Res Lett 34:L14313. doi:10.1029/2007GL029629

Heise W, Caldwell TG, Bibby HM, Bannister SC (2008) Three-dimensional modelling of magnetotelluric data from the Rotokawa geothermal field, Taupo Volcanic Zone, New Zealand. Geophys J Int 173:740–750

Hill JH, Caldwell TG, Heise W, Chertkoff DG, Bibby HM, Burgess MK, Cull JP, Cass RAF (2009) Distribution of melt beneath Mount St Helens and Mount Adams inferred from magnetotelluric data. Nat Geosci. doi:10.1038/NGEO661

Ichihara H, Mogi T, Hase H, Watanabe T, Yamaya Y (2009) Resistivity and density modelling in the 1938 Kutcharo earthquake source area along a large caldera boundary. Earth Planets Space 61:345–356

Jiracek GR (1990) Near-surface and topographic distortions in electromagnetic induction. Surv Geophys 11:163–203

Jones AG (2012a) Distortion decomposition of the magnetotelluric impedance tensors from a one-dimensional anisotropic Earth. Geophys J Int 189:268–284

Jones AG (2012b) Distortion of magnetotelluric data: its identification and removal. In: Chave AD, Jones AG (eds) The magnetotelluric method theory and practice. Cambridge University Press

Jones AG, Groom RW (1993) Strike angle determination from the magnetotelluric impedance tensor in the presence of noise and local distortion: rotate at your peril. Geophys J Int 113:524–534

Jones AG, Chave AD, Egbert GD, Auld D, Bahr K (1989) A comparison of techniques for magnetotelluric response function estimation. J Geophys Res 94:14201–14214

Key K, Constable S (2011) Coast effect distortion of marine magnetotelluric data: insights from a pilot study offshore northeastern Japan. Phys Earth Planet Int 184:194–207

Koyama T (2009) Possibility of three-dimensional magnetotelluric (MT) Inversion by Using MT Phase Tensor data, Paper 107-WED-P1700-1278. In: Proceedings of the 11th scientific assembly, August 23–30, Sopron, Hungary

Lilley FEM (1998a) Magnetotelluric tensor decomposition: Part I. Theory for a basic procedure. Geophysics 63(6):1885–1897

Lilley FEM (1998b) Magnetotelluric tensor decomposition: Part II. Examples of a basic procedure. Geophysics 63(6):1898–1907

Lilley FEM (2012) Magnetotelluric tensor decomposition: insights from linear algebra and Mohr diagrams. In: New achievements in geoscience (Ed: Hwee-Sam Lim) doi: 10.5772/2066. href = "http://www.intechopen.com/books/new-achievements-in-geoscience"title = "New Achievements in Geoscience" > New Achievements in Geoscience

Lilley FEM, Weaver JT (2010) Phases greater than 90 degrees in MT data: analysis using dimensionality tools. J Appl Geophys 70:9–16

Marti A, Queralt AP, Jones A, Ledo J (2005) Improving Bahr's invariant parameters using the WAL approach. Geophys J Int 163:38–41

Martí A, Queralt P, Ledo J, Farquharson C (2010) Dimensionality imprint of electrical anisotropy in magnetotelluric responses. Phys Earth Planet Int 182:139–151

McNeice GW, Jones AG (2001) Multisite, multifrequency tensor decomposition of magnetotelluric data. Geophysics 66:158–173

Moorkamp M (2007) Comment on 'The magnetotelluric phase tensor' by T. Grant Caldwell, Hugh M. Bibby and Colin Brown. Geophys J Int 171:565–566

Pankratov OV, Kuvshinov AV (2010) Fast calculation of the sensitivity matrix for responses to the earth's conductivity: general strategy and examples. Izvestiya-Phys Solid Earth 46:788–804

Parker RL (2010) Can a 2-D MT frequency response always be interpreted as a 1-D response? Geophys J Int 181:269–274

Patro P, Uyeshima M, Siripunvaraporn W (2012) Three-dimensional inversion of magnetotelluric phase tensor data. Geophys J Int manuscript GJI-S-10-0276L.R3

Pek J, Santos FAM (2002) Magnetotelluric impedances and parametric sensitivities for 1-D anisotropic layered media. Comp Geosci 28:939–950

Pous J, Martinez Poyatos D, Heise W, Santos FM, Galindo-Zaldivar J, Ibarra P, Pedrera A, Ruiz-Constan A, Anahnah F, Goncalves R, Mateus A (2011) Constraints on the crustal structure of the internal Variscan Belt in SW Europe: a magnetotelluric transect along the eastern part of Central Iberian Zone, Iberian Massif. J Geophys Res 116:B02103. doi:10.1029/2010JB007538

Roux E, Moorkamp M, Jones AG, Bischo M, Endrun B, Lebedev S, Meier T (2011) Joint inversion of long-period magnetotelluric data and surface-wave dispersion curves for anisotropic structure: application to data from Central Germany. Geophys Res Lett 38:L05304. doi:10.1029/2010GL046358

Schaefer A, Houpt L, Brasse H, Hoffmann N, EMTESZ Working Group (2011) The North German conductivity anomaly revisited. Geophys J Int 187:85–98. doi:10.1111/j.1365-246X.2011.05145.x

Selway K, Thiel S, Key K (2012) A simple 2-D explanation for negative phases in TE magnetotelluric data. Geophys J Int 188:945–958

Siripunvaraporn W, Egbert G, Lenbury Y, Uyeshima M (2005) Three-dimensional magnetotelluric inversion: data-space method. Phys Earth Planet Inter 150:3–14

Smith JT (1995) Understanding telluric distortion matrices. Geophys J Int 122:219–226

Thiel S, Heinson G, Gray DR, Gregory RT (2009) Ophiolite emplacement in NE Oman: constraints from magnetotelluric sounding. Geophys J Int 176:753–766

Unsworth M, Soyer W, Tuncer V, Wagner A, Barnes D (2007) Hydrogeologic assessment of the Amchitka Island nuclear test site (Alaska) with magnetotellurics. Geophysics 72:B47–B57

Wannamaker PE, Hasterok DP, Johnston JM, Stodt JA, Hall DB, Sodergren TL, Pellerin L, Maris V, Doerner WM, Groenewold KM, Unsworth MJ (2008) Lithospheric dismemberment and magmatic processes of the Great Basin-Colorado Plateau transition, Utah, implied from magnetotellurics. Geochem Geophys Gesosys 9:Q05019. doi:10.1029/2007GC001886

Weaver JT, Lilley FEM (2004) Using Mohr circles to identify regional dimensionality and strike angle from distorted magnetotelluric data. Explor Geophys 35:251–254

Weaver JT, Agarwal AK, Lilley FEM (2006) The relationship between the magnetotelluric tensor invariants and the phase tensor of Caldwell, Bibby, and Brown. Explor Geophys 37:261–267

Weidelt P, Chave AD (2012) The magnetotelluric response function. In: Chave AD, Jones AG (eds) The magnetotelluric method theory and practice. Cambridge University Press

Weidelt P, Kaikkonen P (1994) Local 1-D interpretation of magnetotelluric B-polarization impedances. Geophys J Int 117:733–748

Xiao Q, Cai X, Xu X, Liang G, Zhang B (2010) Application of the 3D magnetotelluric inversion code in a geologically complex area. Geophys Prosp 58:1177–1192

Xiao Q, Zhao G, Dong Z (2011) Electrical resistivity structure at the northern margin of the Tibetan Plateau and tectonic implications. J Geophys Res 116:B12401. doi:10.1029/2010JB008163

Yamaguchi S, Ogawa Y, Fuji-ta K, Ujihara N, Inokuchi H, Oshiman N (2010) Audio-frequency magnetotelluric imaging of the Hijima fault, Yamasaki fault system, southwest Japan. Earth Planet Space 62:401–411

Zhang P, Pedersen LB, Maresthal M, Choteau M (1993) Channeling contribution to tipper vectors: a magnetic equivalent to electrical distortion. Geophys J Int 113:693–700